



Defect engineering of Czochralski single-crystal silicon

T. Sinno^{a,*}, E. Dornberger^b, W. von Ammon^b, R.A. Brown^c, F. Dupret^d

^aDepartment of Chemical Engineering, University of Pennsylvania, Philadelphia, PA 19104-6393, USA

^bWacker-Siltronic AG, D-84479 Burghausen, Germany

^cDepartment of Chemical Engineering, Massachusetts Institute of Technology, Cambridge, MA 02139, USA

^dCESAME, Universite Catholique de Louvain, 4 av.G. Lemaitre, B-1348 Louvain-la-Neuve, Belgium

Accepted 4 May 2000

Abstract

Modern microelectronic device manufacture requires single-crystal silicon substrates of unprecedented uniformity and purity. As the device feature lengths shrink into the realm of the nanoscale, it is becoming unlikely that the traditional technique of empirical process design and optimization in both crystal growth and wafer processing will suffice for meeting the dynamically evolving specifications. These circumstances are creating more demand for a detailed understanding of the physical mechanisms that dictate the evolution of crystalline silicon microstructure and associated electronic properties. This article describes modeling efforts based on the dynamics of native point defects in silicon during crystal growth, which are aimed at developing comprehensive and robust tools for predicting microdefect distribution as a function of operating conditions. These tools are not developed independently of experimental characterization but rather are designed to take advantage of the very detailed information database available for silicon generated by decades of industrial attention. The bulk of the article is focused on two specific microdefect structures observed in Czochralski crystalline silicon, the oxidation-induced stacking fault ring (OSF-ring) and octahedral voids; the latter is a current limitation on the quality of commercial CZ silicon crystals and the subject of intense research. © 2000 Published by Elsevier Science S.A.

Keywords: Czochralski silicon; Point defects; Microdefects; OSF-ring; Voids; Defect engineering

1. Introduction

The crystalline silicon wafers that form the substrates for modern microelectronic devices are perhaps the most perfect and well-characterized mass-produced material produced today. This silicon is grown by solidification from the melt using modern, large-scale variants of the method first introduced by Czochralski [1] for the crystal growth of small-diameter crystals for laboratory experiments. Today, silicon boules 300 mm in diameter are routinely grown weighing 250 kg. The large-scale industrial processing equipment used in silicon crystal growth rivals other modern materials processing equipment in cost and complexity.

The purity and crystallographic perfection make semiconductor silicon even more remarkable. Besides oxygen, this material has impurity levels below or near detectable limits, depending on the impurity species, and is a single crystal with no continuous dislocations or grain boundaries. Within these bounds crystalline silicon is anything but a simple material. Since the 1960s it has been become increasingly clear that crystalline silicon contains a plethora of microdefects. The variety of these defects seems to be ever increasing as the methods for experimental identification have progressed

* Corresponding author.

from the first methods of etching and visual detection to the applications of light scattering and transition electron microscopy in use today. Moreover, the effect of these microdefects, nucleated and grown during crystal growth, on subsequent device processing and or microelectronic device performance is becoming clear. As microdevices increase in size and complexity and the feature sizes for these devices decrease, the premium on control of microdefects in crystalline silicon becomes more critical to commercial success.

Traditionally, progress in the optimization and control of Czochralski crystal growth of silicon has come from empirical experimentation based on establishing the causal relationships between the characterized material — either as grown or after some subsequent annealing and processing — and the design and operation of the crystal growth system. Typical control parameters include; the design of the heat transfer environment in the furnace to control the cooling rate of the crystal, design and control of the crystal pull rate as a parameter in setting the temperature field in the crystal, and the residence time of the crystal in the temperature distribution, and operating features to control the dissolution of oxygen into the melt from the surrounding quartz crucible to control the oxygen in the crystal and subsequent oxide precipitation. Although amazingly successful, the empirical approach has become more limited as finer control is being demanded of microdefects and the cost of experiments performed on extremely large Czochralski systems has risen dramatically. Continuing to engineer large-scale crystal systems with traditional experimental empiricism seems impractical.

The goal of this paper is to present an overview of the roles of mathematical modeling, analysis and numerical simulation in modern defect engineering of crystal growth of single crystal silicon. Numerical simulation has been used for some time in materials processing to predict the linkage between system design and operating conditions and continuum properties, such as the temperature field in all components of the system, the flow field in the melt and the distribution of impurities. Thermocapillary models for transport processes in the Czochralski process are reviewed in Section 3 as they pertain to the calculations discussed here. Although these calculations are very useful for system design and operation, they fall short of really linking simulation with the inherent quality of the material. This link, between processing conditions and the microscopic structure of the material, is the goal of silicon defect engineering and a focus of the presentation here. Our goal is to demonstrate the success of a comprehensive framework, which combines modeling over several physical scales with detailed experimental characterization to give a robust and evidently realistic picture of the microstructure of semiconductor silicon.

One of the main purposes of this paper is to show how many of the commonly observed microdefects in silicon can be explained quantitatively in terms of the equilibrium, transport and reaction of native point defects — vacancies and self-interstitials. These point defects, ever present at finite temperature, diffuse, convect and react in the crystal and lead to supersaturation of one species or the other, depending on the details of the temperature distribution in the crystal and processing conditions. As the crystal cools, the supersaturation drives aggregation into microdefects formed from either vacancies, in the form of voids, or self-interstitials, in the form of clusters, stacking faults, and dislocation loops. The atomistic processes of individual point defects, of point defect recombination, and of the addition of point defects to clusters become the basis for building mesoscale equilibrium and kinetic description of point defect dynamics. This framework is used in Section 2 to develop continuum-scale models of point defect transport, reaction and aggregation and to estimate the values of the thermophysical properties that describe individual point defect properties.

The application of defect dynamic analysis is demonstrated in Sections 4 and 5 through two examples. In Section 4 the defect dynamics leading to the well characterized oxidation-induced stacking fault ring (OSF-ring) in Czochralski silicon is studied and shown to be linked to the delicate

balance between vacancies and self-interstitials that occurs in the crystal close to the melt/crystal interface, near the melting temperature. To a first approximation, the location of the OSF-ring can be predicted entirely in terms of the supersaturation of point defects and the temperature field near the solidification front. In Section 5, the analysis is extended to include the aggregation of excess vacancies into voids using self-consistent models of point defect dynamics and aggregation. Detailed numerical simulation is used to predict the density and size distribution of voids. The results are compared directly with experimental measurements and demonstrate the predictive quality of the analysis. We conclude with perspectives on future developments.

2. Defect physics in semiconductor silicon

The central role of intrinsic point defects as building blocks for many microdefect species in silicon motivates a detailed understanding of their equilibrium and transport properties; e.g. their equilibrium concentrations, diffusivities, recombination rates and aggregation kinetics. These properties play an essential role in determining the quality of single-crystal silicon during growth [2,3] and device processing [4]. The high temperature properties are especially important because of the role of thermally activated diffusion and reaction processes in the nucleation and aggregation of precipitates formed during thermal annealing of crystals. The term *point defect dynamics* is used to refer to the various microscopic processes for point defects in silicon.

The basic physical concepts necessary to understand quantitatively these phenomena are introduced in Section 2.1. The building blocks for these models are brought together in Section 2.2 into a continuum description of point defect and microdefect dynamics in the form of a system of coupled partial differential equations. The obvious usefulness of such models has created an urgent need for measurement and computation of the thermophysical property information required for numerical evaluation. A brief overview of the major avenues for these studies also is presented in Section 2.2.

2.1. Point defect dynamics

2.1.1. Point defect formation

The intrinsic point defects, namely the self-interstitial and the vacancy, are present in finite concentrations in all crystalline materials at finite temperature, due to free energy considerations [5]. The free energy of a lattice containing n point defects distribution across N lattice sites is written as

$$G = G_0 + nG^f - kT \ln \frac{N!}{(N-n)!n!}, \quad (2.1)$$

where, G^f is the free energy of formation of point defects, G_0 the perfect crystal free energy, N denotes the number of lattice sites, and the last term gives the configurational entropy. This term lowers the total free energy and provides the thermodynamic driving force for the formation of a finite number of point defects. An expression for the equilibrium state is derived by minimizing Eq. (2.1) with respect to n . Using a concentration representation the equilibrium state can be written as

$$C^{\text{eq}}(T) = C_s \exp\left(-\frac{G^f}{kT}\right), \quad (2.2)$$

where C_s is the lattice site density. The equilibrium concentration is written in a more transparent form by separating the entropic and enthalpic contributions, so that

$$C^{\text{eq}}(T) = C_s \exp\left(\frac{S^{\text{f}}}{k}\right) \exp\left(-\frac{H^{\text{f}}}{kT}\right). \quad (2.3)$$

The equilibrium concentration of each point defect species is then strongly dependent on temperature and couples the time-dependent evolution of the thermal field during silicon crystal growth and processing to the development of supersaturated point defects. This supersaturation is the principle driving force for the formation of microdefects and for other processes such as point defect recombination, described below.

2.1.2. Point defect diffusion

A crucial aspect of microdefect formation in silicon processing is the rapid solid-state diffusion found at high temperatures. Without sufficiently rapid diffusion, point defects would not have the time during typical growth and processing thermal schedules to interact and form the microdefects discussed in Section 1. Point defect diffusion is typically understood to be a thermally activated jump process, and can be mathematically expressed, using rate theory, in terms of a jump rate [6]:

$$D(T) = D_0 \exp\left(-\frac{H_m}{kT}\right). \quad (2.4)$$

where D_0 is related to an attempt frequency and H_m is an activation energy barrier for migration which represents the enthalpy difference of the system between the equilibrium and saddle-point (highest energy) configurations [5,7]. Most experimental measurements as well as computations correlate results with such an expression to reduce the number of parameters required in the mathematical description of diffusion.

2.1.3. Point defect recombination

Point defect recombination is the simplest interaction between point defects and is very important for releasing thermodynamic stresses within the silicon bulk. The reversible recombination process can be written as



where 0 refers to a perfect lattice atom. The effect of this reaction is to produce an interdependency between self-interstitial and vacancy distributions. Despite the importance of this reaction, its kinetics are still poorly understood [4,8].

An expression for the **recombination rate** is developed using diffusion-limited reaction theory [9] where the total barrier to recombination is a function of the mobility of the point defects and a free energy activation barrier:

$$k_{\text{IV}}(T) = 4\pi a_{\text{r}}(D_{\text{I}} + D_{\text{V}}) \exp\left(-\frac{\Delta G_{\text{IV}}}{kT}\right), \quad (2.6)$$

where a_{r} is an effective capture radius, D_X the diffusivity of point defect species X , and ΔG_{IV} represents a free energy barrier against recombination. The nature of the recombination barrier is

poorly understood [10]. An activation barrier can be generally written in terms of enthalpic and entropic components [11]

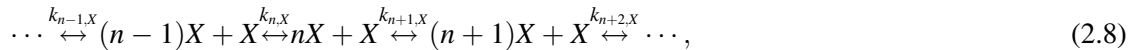
$$\Delta G_{IV}(T) \equiv \Delta H_{IV}(T) - T\Delta S_{IV}(T), \quad (2.7)$$

however, quantitative estimates for these contributions are very difficult to obtain, but there is evidence that the recombination barrier is small (below 1.0 eV) and that point defect recombination at temperatures near the melting temperature is extremely rapid [12,13].

It has long been postulated that so-called point defects are not really point-like at elevated temperatures but tend to exhibit a cloud-like structure [11,14]. This concept has lead to the realization of a large entropy of formation for high temperature point defects which must be at least partially released upon recombination. Large entropies of formation have been computed by atomistic simulation [15] and these results are used to construct an estimate for a recombination barrier in our calculations, described in detail in the following sections.

2.1.4. Point defect aggregation

Point defect aggregation is also driven by supersaturation and is responsible for the formation of microdefects in silicon. While recombination refers to the interaction of a self-interstitial with a vacancy, aggregation is typically used to refer to the clustering of like species. The theory of homogeneous nucleation and aggregation is very well developed within this context [16,17] and a common approach is to consider a system of mobile monomers (point defects) that aggregate by homogeneous nucleation under a supersaturation driving force. Dimers, trimers and larger aggregates are usually assumed to be immobile and dilute in solid state systems, so that aggregate coalescence is not an important process, and growth and dissolution occur only via monomer addition and emission, respectively. Under these conditions, a sequence of reversible reactions are written for the dynamical evolution of cluster sizes [13]



where X represents a single point defect, and nX a cluster of n point defects. Expressions for each of the aggregation steps are obtained by considering the forward and backward aggregation rates for each cluster size. The reaction represented in Eq. (2.8) by $k_{n,X}$ can be decomposed into two steps; the growth of clusters of size $(n-1)$ to size n (denoted by $k_{n,X}^f$), and the dissolution of clusters of size n to clusters of size $(n-1)$ (denoted by $k_{n,X}^b$). These reactions are represented as bimolecular and unimolecular processes, respectively:

$$k_{n,X}^f = \alpha_{n,X} C_{(n-1)X} C_X, \quad (2.9)$$

and

$$k_{n,X}^b = \beta_{n,X} C_{nX}. \quad (2.10)$$

Expressions for $\alpha_{n,X}(T)$ and $\beta_{n,X}(T)$ also are developed using diffusion-limited reaction theory. The total free energy of a system containing a distribution of point defects and their aggregates can be written as

$$G_X = G_X^0 + \sum_n z_n G_X^f(n) - kT \ln \Omega, \quad (2.11)$$

where G_X^0 is a reference free energy, $G_X^f(n)$ denotes the non-configurational free energy of formation of an aggregate, z_n the number of aggregates of size n and Ω is the number of ways clusters can be distributed across lattice sites [17]. Assuming that clusters are distributed dilutely within the lattice, the free energy change required to grow a cluster by the incorporation of a monomer is given by

$$\Delta G_{n \rightarrow n+1, X} \equiv G_X^f(n+1) - G_X^f(n) - kT \left(\frac{C_X}{C_X^{\text{eq}}} \right). \quad (2.12)$$

As in Section 2.1.3, the aggregation rate is written using diffusion limited aggregation theory in the form

$$k_{r, X}(n, \bar{r}) = \frac{4\pi r_v^2 D_X}{\delta} \exp\left(-\frac{\Delta G_{n \rightarrow n+1, X}}{kT}\right), \quad (2.13)$$

where δ is the jump distance required for the point defect to attach to the cluster, and is taken to be approximately one lattice spacing. The free energy associated with a cluster, $G_X^f(n)$, is written classically as a sum of surface and volume contributions so that

$$\Delta G_X^f(n) = 4\pi r_c^2 \sigma_X + \frac{4}{3}\pi r_c^3 \Delta G_{b, X} \quad (2.14)$$

where r_c is the radius of a spherical cluster, σ_X represents the surface free energy per unit area, and $\Delta G_{b, X}$ is the bulk energy per unit volume. Eq. (2.14) assumes that each aggregate has spherical morphology and macroscopic dimensions. For very small clusters, such a representation is not valid and alternative methods must be used. Because of the difficulty in observing experimentally such species, attempts at determining small cluster free energies are focused entirely on atomistic [18] and electronic structure calculations [19].

2.2. General defect dynamics model framework

2.2.1. Conservation equation development

All quantitative models of defect dynamics in crystal growth and during wafer processing are largely based on the phenomena described in Section 2.1. For both cases, the primary goal is to develop a model that will predict accurately the distribution of point defects and microdefects as a function of operating conditions, typically the thermal environment, and in the case of crystal growth, the crystal pulling rate V or the rate at which the crystal translates through the temperature field determined within the furnace. For point defects, the species conservation equations are written as [12]

$$\frac{DC_I}{Dt} = \nabla \cdot \left(D_I(T) \nabla C_I - \frac{D_I(T) C_I Q_I^*}{kT^2} \nabla T \right) - k_{IV}(C_I C_V - C_I^{\text{eq}} C_V^{\text{eq}}) - \frac{\partial}{\partial t} \int_2^\infty n f_I(n, \bar{r}) dn, \quad (2.15)$$

$$\frac{DC_V}{Dt} = \nabla \cdot \left(D_V(T) \nabla C_V - \frac{D_V(T) C_V Q_V^*}{kT^2} \nabla T \right) - k_{IV}(C_I C_V - C_I^{\text{eq}} C_V^{\text{eq}}) - \frac{\partial}{\partial t} \int_2^\infty n f_V(n, \bar{r}) dn, \quad (2.16)$$

for self-interstitials and vacancies, respectively. In Eqs. (2.15) and (2.16)

$$\nabla = \bar{e}_r \frac{\partial}{\partial r} + \bar{e}_z \frac{\partial}{\partial z}$$

for an axisymmetric system. The substantial derivative, $D/Dt \equiv (\partial/\partial t + V\partial/\partial z)$, is defined here as the rate of change of concentration at a point *moving with the velocity of the growing crystal*. Also, $Q_{1,V}^*$ are the reduced heats of transport for point defects [20] which describe the rate of material flow due to a gradient in temperature. The last term in each balance equation shown above represents the incorporation of point defects into clusters of all possible sizes. Here, $f_X(n, \bar{r})$ is the concentration of clusters of point defect X , and size n at a given position \bar{r} , within the crystal. Eqs. (2.15) and (2.16) have been used extensively in the defect dynamics simulation literature [21–23]. The main differences between various investigations are typically in the estimates for the various thermophysical properties and in the interpretation of experimental data for microdefect dynamics, particularly the OSF-ring [22]. The latter issue is discussed in detail in Section 4.

Cluster balance equations are developed using Master Equations for each aggregate size and are written for self-interstitial and vacancy clusters as

$$\frac{DC_{n,X}}{Dt} = J_{n,X} - J_{n+1,X}, \quad (2.17)$$

where $J_{n,X}$ is the nucleation flux of species X , and is given by

$$J_{n,X} = g_X(n-1)C_{n-1,X} - d_X(n)C_{n,X}, \quad (2.18)$$

where $g_X(n)$ and $d_X(n)$ represent the growth and dissolution rates for clusters of size n , respectively. Models for describing $g_X(n)$ and $d_X(n)$ are based on the surface reaction rates and local monomer concentrations at the cluster surfaces. Assuming rapid kinetics, the growth rate is written as

$$g_X(n) = k_{r,X}(n, \bar{r})C_X(r_c), \quad (2.19)$$

and the dissolution rate as

$$d_X(n) = k_{r,X}(n, \bar{r})C_X^{\text{eq}}(r_c), \quad (2.20)$$

where C_X and C_X^{eq} are the monomer concentration and equilibrium concentrations, respectively. The rapid consumption of monomers in the vicinity of a cluster leads to a diffusion-limited regime in which a mesoscopic concentration profile about the cluster is established. The actual monomer concentration is obtained by setting the cluster growth rate equal to the arrival flux of monomers at steady state. The equilibrium concentration of monomers at the surface of the cluster is obtained by minimizing the free energy of the cluster with respect to its size according to the classical analysis of Lifshitz and Slyozov [24], to give

$$C_X^{\text{eq}}(r_c) = C_X^{\text{eq}}(\infty) \exp\left(\frac{\partial G_X^f(n)/\partial n}{kT}\right). \quad (2.21)$$

The size distribution of clusters observed in bulk silicon makes a Master Equation representation unfeasible for numerical solution. A common approach is the use of an approximation in which the Master Equations are reduced into a single Fokker–Planck equation (FPE) by assuming that the cluster size can be represented continuously [25]. This approximation has been shown to be a good approximation for clusters containing more than about 10 or 20 monomers [26]. The FPE can now be written in terms of a continuous nucleation flux ($I_{n,X}$)

$$I_{n,X}(\bar{r}) \equiv g_X(n-1)f_X(n-1, \bar{r}) - d_X(n)f_X(n, \bar{r}), \quad (2.22)$$

where $f_X(n, \bar{r})$ is a continuous function of size and space, and is given by

$$\frac{Df_X}{Dt} = \frac{\partial}{\partial n} \left(A_X(n)f_X - B_X(n) \frac{\partial f_X}{\partial n} \right), \quad (2.23)$$

and

$$A_X(n) = g_X(n) - d_X(n) - \frac{\partial B_X(n)}{\partial n}, \quad (2.24)$$

and

$$B_X(n) = \frac{1}{2}(g_X(n) + d_X(n)). \quad (2.25)$$

2.2.2. Boundary conditions

The proper formulation of the model represented by Eqs. (2.15)–(2.25), requires mathematically appropriate boundary conditions for all species on all boundaries of the system. The representation of the boundary conditions during crystal growth and device processing remains as one of the more uncertain aspects of defect dynamics modeling. The mathematically parabolic partial differential equations (including diffusion) for point defects require boundary conditions on all crystal surfaces. For crystal growth from the melt, point defects are usually assumed to be incorporated in equilibrium concentrations across the melt/solid interface

$$C_X(\text{melt/solid}) = C_X^{\text{eq}}(T_m) \quad (2.26)$$

There is little evidence in the literature to support or discredit this assumption. The work of Van Siclen and Wolfer [27] which models the non-equilibrium entrapment of point defects considers much higher growth rates than are typically used in commercial silicon crystal growth and we use this as an indication that the assumption of equilibrium is reasonable in this application. Alternatively, it is important to mention that the microscopic growth rate can reach much higher rates as the crystal actually grows in stepwise fashion, and the growth rate V considered above in the continuum model is only the average value. However, there is simply not enough information available to refine the equilibrium assumption in Eq. (2.26) and it is used for all analysis described in this article.

Greater variety is observed in models for the boundary conditions on the point defect concentrations at the gas/crystal surfaces, which are particularly important in the case of wafer processing situations. The general boundary condition appropriate at these surfaces is the inhomogeneous mixed, or Robin, condition given by [28]

$$-D_X \nabla C_X + k_X^s (C_X - C_X^{\text{eq}}) = g_X^s, \quad (2.27)$$

where k_X^s is the surface rate of defect annihilation (or creation) and g_X^s is an additional surface flux that describes point defect absorption or injection from the bulk, usually attributed to the chemical environment present at the surface [4]. While Eq. (2.27) represents a general case, it is hard to implement because of the lack of data available for k_X^s and g_X^s . Accordingly, defect dynamics modeling efforts to date have assumed that one of two limits prevail: either the surface reaction is very fast relative to diffusion so that equilibrium conditions prevail at the surface, or the surface is sufficiently far from the bulk that the effects of the surface do not matter and $k_X^s = 0$ is imposed. The

latter is used predominantly for large diameter crystal growth simulations [12], while the former has been found to be closer to reality in wafer processing simulations.

The mathematically hyperbolic equations (for $V \neq 0$) for the dynamics of aggregates require boundary conditions only on the species concentrations at the melt/crystal interface. All aggregate species are presumed to be at zero concentration at the melt/solid interface, an assumption usually argued based on the diluteness of point defects and the fact that the equilibrium concentrations of aggregates is very small.

2.3. Thermophysical property estimation

It is generally agreed that the Achilles heel of defect dynamics modeling in silicon is in the critical area of defect thermophysical property estimation. By thermophysical properties, we refer to defect diffusivities, equilibrium concentrations, aggregation rates, and recombination rates. The reasons for this situation stem entirely from the sensitivity of the model represented by Eqs. (2.15)–(2.25) to these properties. These properties have been measured experimentally and computed by simulation numerous times and while there is now converging consensus on their values, at least semi-quantitatively, the degree of uncertainty is still far too large for us to specify them *independently* of a model and still obtain reasonable agreement with experiment. Here, we will present a brief overview of the various methods and techniques used to measure these elusive properties, first by discussing experimental measurements and then by describing attempts at calculation of these properties.

2.3.1. Experimental determination of thermophysical properties

No experimental technique currently exists that allows a clear, direct measurement of self-interstitial and vacancy properties. What are measured are indirect effects such as the diffusion of dopant atoms or the growth rates of microdefects under specified thermal conditions and dopant concentrations. Diffusion-reaction models with the point defect properties as adjustable parameters are then used to fit the experimental data. In order for this approach to work, the important physical and chemical processes governing point defect transport and reaction must be well understood and mathematically characterized. In addition, the experimental data must be accurate and comprehensive enough to allow the simultaneous fitting of several thermophysical properties associated with both the diffusing species and the point defects.

There are several commonly used experimental techniques for estimating intrinsic point defect transport and equilibrium properties in silicon. Dopant diffusion experiments monitor an impurity diffusion profile as a function of time and temperature. An example is the diffusion of gold [29,30] in silicon. Gold in silicon generally exists in the substitutional state (it preferentially occupies silicon lattice sites) but is transported within the lattice in the interstitial state [31]. Thus, diffusion requires that a substitutional gold atom is first transformed into the interstitial state where it is mobile and then for it to redissolve into the substitutional state. The coupling of the native point defect and gold diffusion profiles yields an indirect probe of point defect properties. Other metals also are used in similar gettering experiments; examples are zinc used by Bracht et al. [32], and platinum by Zimmermann and Rysse [29].

A very different set of experiments is based on characterizing the growth rates of geometrically well-defined microdefects. In particular, surface oxidation of silicon wafers by annealing in steam at high temperature has been used extensively to estimate point defect properties using the same general methodology as described above. It has been found that surface oxidation leads to the generation and growth of interstitial-type oxidation-induced stacking faults (OSF) [33] with

morphologies that have been well characterized by transmission electron microscopy [34]. These stacking faults result because of self-interstitial injection due to the growth of the oxide layer on the surface of the wafer and measurements of the OSFs growth rates can then lead to information about the rate of self-interstitial diffusion and concentration when coupled with a model for these processes.

There are a few inherent limitations of most of the experimental approaches described above. The first limitation is that they all rely on a fitting model to extract several parameters simultaneously; this process can lead to non-uniqueness in the extracted parameter values. The second, and perhaps most important, consideration is that the initial conditions for the experiments are ignored, no account is taken of the distribution of as-grown microdefects in the material. The material supplied for the diffusion experiments is likely to contain widely varying concentrations of defect aggregates, ranging from voids to self-interstitial clusters to oxygen precipitates. At the temperatures used in diffusion and stacking fault growth experiments, these defects will tend to interact strongly with the point defect concentration and hence affect the diffusion profiles and the thermophysical properties obtained in the parameter fitting. In other words, in order to obtain a realistic simulation of metal diffusion, it would be necessary to perform self-consistent simulations of the crystal growth conditions, or at least measure carefully the defect size distribution and include it in the diffusion model.

A more direct experimental approach to measure vacancy formation enthalpies [35] has been the use of positron annihilation, which gives a relatively direct method for measuring concentrations of charge neutral vacancies. Positrons injected into the lattice annihilate with lifetimes characteristic to a particular mechanism. In the case of the neutral vacancy, the formation energy can be measured quite accurately once the correct lifetime peak has been assigned. However, the quantitative interpretation of positron annihilation data is quite involved and uncertainty in these results also exists.

2.3.2. Theoretical estimation of thermophysical properties

A frequently used alternative to experimental measurement is the estimation of the properties using atomistic simulation, based primarily on the Monte Carlo or molecular dynamics methods [36]. The advantage of simulation lies in the explicitness of the results, making direct estimation of thermodynamic properties straightforward, in principle. For example, dynamical simulations track the evolution of atomic coordinates in real time, giving direct information about the mobility of a defect without the need to measure an indirect property. The caveat '*in principle*' is necessary due to the dependency of these simulations on the specification of an interatomic force field, which describes the forces between atoms as a function of their relative positions.

The appropriate choice of interatomic potential for crystalline silicon is vital to obtain quantitatively accurate results. The methods for calculating interatomic forces for silicon range from relatively simple classical interatomic potentials based solely on the positions of neighboring atoms to quantum mechanical methods that solve, to varying degrees of accuracy, for the electronic structure of the atomic system. The choice of method is based on several considerations; while fully ab initio quantum mechanical calculations [37,38] are most accurate, these are computationally demanding, limiting the system size and time scale for any simulation; calculations of this type are not practical for large clusters of atoms or extended defects. These limitations motivate the use of empirical interatomic potentials especially for the simulation of larger defect clusters that require many atoms and longer simulation times. Empirical potentials are generally constructed by postulating an analytical form for the potential energy as a function of atomic coordinates with several adjustable parameters that are fit to known physical properties, such as melting points, lattice

parameters, cohesive energies, and the diamond structure bulk modulus. Examples of such forms are the Stillinger–Weber [39] (SW) potential, the Tersoff [40,41] potentials, and the environment-dependent interatomic potential (EDIP) [42,43]. While the motivation for the analytic form of each potential is different, they each share the same philosophy discussed above.

There have been numerous calculations performed using these potentials and others. A few examples of such studies are those by Maroudas et al. [7], Schober [44], and Balamane et al. [45]. Detailed comparisons of each for prediction of various properties have been performed and summarized in the latter. In general, it is difficult to tout the superiority of a particular potential form over the others, as each have individual areas of strengths and weaknesses. Despite these shortcomings, the results for point defect properties are at least semi-quantitatively accurate and often provide insight into mechanistic aspects of point defect migration and structure.

While empirically derived interatomic potentials are useful because of their relative simplicity (and therefore low computational requirements), they do not consider electronic structure contributions explicitly, instead relying on an ad hoc analytical expression with adjustable parameters to capture the essential features of electronic bonding. So-called *ab initio* calculations are based on parameter-free methods that solve an approximate representation of the valence electron potential [46]. Dynamical, finite temperature calculations were made feasible by the development of the Car-Parinello molecular dynamics method [37] and the local density approximation (LDA). Calculations based on this approach can consider $O(10^2)$ atoms evolving for about $O(10^{-12})$ seconds. These limits are just enough to allow for the relaxation of single point defects in materials such as silicon but until significantly faster computers or numerical methods are found, fully *ab initio* methods will remain very computationally expensive.

A much cheaper approach to computing electronic band structures is by using the theory of linear combination of atomic orbitals (LCAO) as developed in tight-binding (TB) approximation. Examples of calculations using this technique for computing silicon point defect properties are given by Rasband et al. [47] and Wang et al. [48] and for clusters of vacancies by Bongiorno and Colombo [19].

2.4. System geometry and operating conditions

The final input required by the model given by Eqs. (2.15)–(2.25) describes the macroscopic operating conditions. These are typically given in the form of thermal fields, system geometry, and, in the case, of crystal growth, the pulling rate. Clearly, these inputs are much simpler to approximate in the case of wafer processing, where the thin geometry in the axial direction leads to a constant temperature profile for all time except in the case of rapid thermal annealing treatments. For crystal growth, the situation is far more complicated and much effort has been expended in the modeling and simulation of heat transfer in the Czochralski crystal growth system so that a thermal field within the growing crystal can be specified accurately.

The modeling of heat transfer in the CZ system is described in detail in Section 3. These simulations also attempt to compute the shape of the melt/solid interface because of the strong coupling between the thermal field near the interface and the local geometry. Accurate representation of the physics in this system requires the simultaneous treatment of heat transfer in the entire system and fluid mechanics in the melt.

The results of these calculations, along with estimates for the point defect and cluster thermophysical properties are used to numerically solve Eqs. (2.15)–(2.25) subject to the boundary conditions described in Section 2.2.2. This model is a highly complex, non-linear set of partial differential equations that are essentially three-dimensional at steady state (two spatial dimensions

and one size dimension) and four-dimensional for transient calculations. The numerical solution of these equations is a formidable task and is briefly outlined in the following Section.

2.5. Numerical solution of the defect dynamics model

The numerical solution of Eqs. (2.15)–(2.25) requires sophisticated numerical methods constructed for efficient discretization of variables in space and in the size distribution (the FPE). We do not go into detail here, but refer the reader to Sinno and Brown [49] and to Mori [50]. The discretization of spatial variables in the point defect evolution equations and cluster equations is based typically on either the finite-element or finite-difference methods. The calculations presented below are based on a hybrid method that is optimized to give accuracy and robustness to the calculations. The analysis is restricted to steady-state crystal growth conditions; Mori [50] has extended the analysis to fully time-dependent defect dynamics simulation. The steady-state point defect conservation equations are elliptic partial differential equations that are well suited to discretization using the Galerkin finite-element method. Quadrilateral, bilinear elements are used to discretize the axisymmetric half-plane of the crystal. The rapid cooling of the crystal coupled with the Arrhenius temperature dependence of most of the thermophysical properties leads to boundary layers in the vicinity of the melt/crystal interface and along the crystal/gas surface. These regions are discretized with a more refined mesh than the remaining portion of the crystal.

The FPE and the discrete rate equations for clusters are hyperbolic differential equations in physical space, because of the absence of diffusion. We solve these by the classical streamline upwind finite element method formed by including artificial diffusion [51]. The n -space portion of the FPE is notoriously difficult to solve by traditional methods, both because of the form of the diffusion and drift coefficients and because of the enormous range of n ($1 \leq n \leq 10^{10}$) that must be discretized. The FPE is discretized using a finite difference technique due to Chang and Cooper [52], designed specifically for FPEs. This approach has proven to be both accurate and robust in a variety of calculations.

3. Global heat transfer modeling

The dynamics of point defects and formation of point defect aggregates during crystal growth couples to crystal growth conditions through the temperature field in the crystal and the pull rate of the growing crystal, which determines the thermal history of a material element of the crystal. Tailoring of the temperature field experienced by the crystal is the link that allows control of the microdefect density and type in the as-grown crystal, the goal of defect engineering. This defect engineering requires accurate characterization of the thermal field during crystal growth. Experimental measurements of this temperature field are tedious and expensive. Today, heat transfer simulations based on the finite element method have become sufficiently accurate to be an exceptional tool for calculating this temperature field and designing hot zone configurations in Czochralski crystal growth systems.

In this section the Czochralski crystal growth process is described and the general theory for heat transfer mechanisms in CZ crystal growth are outlined. Most of the elements of the Czochralski system described here are common and are discussed only briefly. The latter part of this section discusses our particular model and gives examples of its predictive capability by direct comparison of calculations to experimental data. These results form the basis for the simulation of microdefect dynamics which is described in the following sections.



Fig. 1. Photograph of a Czochralski furnace with a grown 200 mm crystal (Wacker Siltronic AG).

3.1. The Czochralski silicon crystal growth process

Silicon single crystals for device applications are produced today by the Czochralski method with diameters ranging from 100 to 300 mm and weights up to 250 kg, which is shown in Fig. 1; see [53–56] for details. The first step of the CZ process is to melt semiconductor grade polysilicon chunks in the silica crucibles using heat supplied from the surrounding graphite resistance heater at temperatures above 1400°C. A graphite susceptor is used to support the silica crucible because the crucible becomes soft at high temperatures. The water-cooled steel chamber walls are protected from the hot furnace parts by graphite and graphite felt insulation. Hot zone materials are made from ultra pure graphite, in order to keep the impurity level low in the furnace, particularly the concentrations of heavy metals. The atmosphere in the growth chamber is controlled using an argon gas purge at pressures ranging from 20 to 100 mbar.

After the polysilicon is completely melted and the temperature of the melt is adjusted to be close to the melting temperature, a seed crystal with a chosen crystallographic orientation is contacted with the melt and slowly withdrawn [57]. The seed and crucible are counter-rotated with typical rotation rates of 2–30 rpm. The crystal shape is controlled by the pull rate and the heater power. When the seed crystal comes into contact with the melt, dislocations are generated due to thermal shock. Dislocation free crystals are produced by applying Dash's technique [58], where a very thin seed crystal is grown with a high pull rate. Under these conditions, the dislocations move to the lateral crystal surface and the diffusion controlled climb of dislocations is outpaced by fast pulling. After growth of several centimeters, the seed crystal becomes dislocation free, and the crystal diameter is increased by reducing the pull rate.

After completion of the batch-wise process, the crystal is cut into slices of approximately 1 mm thickness. Lapping, etching and polishing processes follow before the wafers are ready to be used for

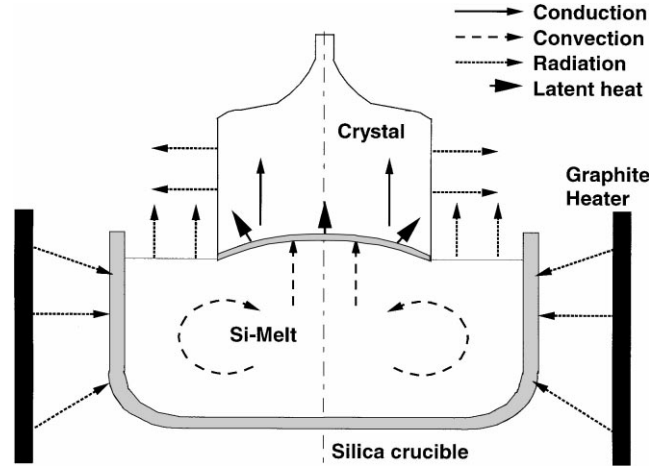


Fig. 2. Heat transport by radiation, convection, conduction and solidification in a CZ furnace.

device applications. In some cases, an epitaxial silicon layer is deposited on the side of the wafer that will be used for building devices.

3.2. Heat transport modes in CZ silicon growth

The CZ silicon crystal growth furnace consists of several solid parts, such as the heater components and the crucible, a liquid phase (the melt), and a gas phase within the furnace enclosures. Heat transport in the growth chamber is shown schematically in Fig. 2, and is governed by the following mechanisms [59]:

1. conduction inside all solid parts,
2. convection and conduction within the melt and inert gas,
3. radiation between components in the furnace enclosures,
4. latent heat release by solidification at the solid/liquid interface,
5. production of heat by heat sources such as the resistance heater.

3.2.1. Conductive heat transport in solids

In the solid parts of the CZ systems, the energy Eq. (3.1) is written as

$$\rho C_p \frac{DT}{Dt} = \nabla \cdot (k(T) \nabla T) + W \quad (3.1)$$

where ρ is the density, C_p the heat capacity, $k(T)$ is generally a non-constant thermal conductivity and W is an external heat source. Boundary conditions on solid surfaces and interfaces in the CZ system depend on the overall geometry and represent contact either with other solid bodies or with a fluid phase. In the case of the former, the temperature and flux are matched, while in the case of contact between the solid and a fluid, a convective heating or cooling condition across the interface is prescribed, and is given by

$$\bar{q} \cdot \bar{n} = h_t(T - T_0) + \text{radiative heat flux}, \quad (3.2)$$

where \bar{q} is the heat flux, h_t is a convective heat transfer coefficient and T_0 the outer coolant

temperature. The radiative heat flux between solid elements in the system is an important mechanism at high temperatures and is discussed in Section 3.3.2.

3.2.2. Heat transport in the melt

Melt convection in industrial-scale silicon crystal growth systems is turbulent and three-dimensional [50]. The onset of turbulence is characteristic of low Pr number fluids where flow instabilities and the transition to turbulence occurs at Grashof (Gr) numbers as low as $O(10^6)$ [60]. The melt flow in industrial silicon crystal growth is within the fully turbulent regime with Gr numbers $O(10^{10}–10^{12})$. These flow conditions lead to two important effects. First, convection in the melt contributes substantially to the efficiency of heat transfer within the system and is an important ingredient in setting the temperature distribution along, and shape of, the melt/crystal interface. Through this interaction, it is a crucial ingredient in determining the point defect dynamics, especially near the interface. Second, convection in the melt controls oxygen transfer by dissolution of the crucible and the transport of oxygen through the melt to the gas and into the crystal.

Direct numerical simulation of such flows is on the edge of what is feasible using large-scale numerical simulation. The application of turbulence models — such as eddy viscosity and $k-\epsilon$ models [61] — offer the advantage of yielding formulations that can be incorporated into thermocapillary models of heat transfer and dopant transfer in the CZ system. Such calculations are under development; see Lipchin and Brown [62,63] for examples of the results of several $k-\epsilon$ models and the incorporation of these turbulence calculations into thermocapillary methods for predicting heat transfer. The extension of these results to prediction of oxygen segregation in the CZ system is described in Lipchin and Brown [64]. These calculations are just beginning to be useful for prediction of temperature field and species transport in large-scale CZ systems.

The calculations reported here are based on a simplified approach that by-passes the need for direct calculation of convective heat transport in the melt by making use of experimental data from the CZ system. This approximate model for heat transport in the melt is discussed in Section 3.3.1.

3.2.3. Heat transport in the gas phase

Convective heat transport by the flowing low pressure argon gas may be neglected in CZ growth of silicon crystals, because of its minor influence on the overall heat transport relative to heater radiation. An estimate of the magnitude of the overall convective heat transport per unit time by the argon gas is of order 0.1 kW for a temperature increase of 1300 K, a flow rate of 1000 NL/h and a pressure of 20 mbar within the furnace. This heat transport is very small compared to the heater power of more than 50 kW.

3.2.4. Heat transport across the solid/liquid interface

Solidification of the melt takes place at the melt/crystal interface and releases the latent heat of solidification. The evolution of the shape of the melt/crystal interface is determined, to a large extent, by the dynamics of the growth process and the crystallographic orientation of the interface. Although almost all models of CZ crystal growth treat heat transfer and the melt/crystal interface as quasi-steady-state properties [65], it is clear that there are short time scale fluctuations that affect solidification. Examples of these are the excursions in pull rate caused by automatic diameter control during growth and cyclic temperature fluctuations that are imposed on the interface by crystal and crucible rotation [66,67].

The energy balance at the melt/crystal interface (i) has three contributions: latent heat release W_i , heat flux from the melt to the interface, q_i^L , and the heat flux from the interface into the crystal

q_i^S . These quantities are related by the interfacial heat balance (Eq. (3.3)) given by

$$q_i^L + W_i = q_i^S. \quad (3.3)$$

Note that W_i increases proportionally with growth rate and an increase of pull rate will generate a more concave interface shape [68]. In general, q_i^L for the melt is a function of buoyancy differences in the melt, which are related to temperature differences, and to crucible and crystal rotation rates [69]. All three contributions can be computed in a self-consistent heat transfer analysis of the CZ system.

3.3. Modeling of the heat transfer in a CZ furnace

Simulation of heat transfer in a complete growth furnace has been used extensively for predicting the thermal history of crystals and the temperature distributions of hot zones. Kobayashi and coworkers [70,71], Arizumi et al. [72] and Miyahara et al. [73] investigated the thermal history of crystals and the shape of the interface by a global heat transfer model including a $k-\varepsilon$ turbulence model. They found that the radial temperature variation near the interface is important for controlling the thermal history in the high temperature range. Crochet et al. [74] Dupret and coworkers [75–77], Brown et al. [78], Atherton et al. [79], Bornside et al. [80] and Derby et al. [81] developed models for CZ and Bridgman furnaces based on finite element methods by taking into account the two-dimensional melt convection and radiation. Derby et al. [82,83] have shown that a quasi-steady-state assumption is valid if a constant crystal diameter is considered. In case of a varying diameter during growth, fully transient models have to be employed.

The dynamics of the CZ process and the response of crystal diameter to pull rate and heater power variations have been investigated by Crowley [84], Hurle et al. [85] and Kim et al. [86]. Hwang et al. [87] applied perturbation methods to study the dynamic behavior of the CZ growth process. Van den Bogaert et al. [88,89] calculated the global time-dependent behavior of CZ growth processes including radiation transfer evolution and investigated the crystal diameter dynamics by applying heater power and pull rate variations. Further heat transfer computations in CZ furnaces have been reported by Ramachandran et al. [90], Williams et al. [91], Hamidi et al. [92] and Anttila et al. [93]. We have used the simulation code ‘FEMAG’ developed by Dupret et al. [76,77] in all our calculations to predict the temperature distribution in the entire CZ furnace.

3.3.1. Modeling of convective heat transfer

The prediction of microdefect formation in the growing crystal requires accurate prediction of the temperature field in the crystal, especially near the melt/crystal interface. Solution of the melt convection problem is avoided in calculations presented here by the use of an empirical model for the calculation of the heat transfer from the silicon melt to the crystal. The approach is described below.

The conduction dominated version of the software-code FEMAG [76] was used to compute temperature distributions throughout a crystal growth furnace by modeling heat transfer by conduction in all solid phases and by radiation in the furnace enclosure. Heat transfer in the melt is approximated by solving the energy equation in the melt without convection, but with an effective thermal conductivity to model the effect of convective transport. If the molecular thermal conductivity is used, neglecting any effect of convective transport, the resulting heat flux from the melt to the crystal is inaccurate, as is the shape of the melt/crystal interface. The effective

conductivity k_{eff} used in the energy equation accounts empirically for convective heat transport, as is the approach in an eddy-viscosity turbulence model, where a turbulent conductivity is added to the molecular conductivity [61].

The effective conductivity (k_{eff}) used here was determined by comparing computed temperature distributions in the melt and interface shapes with experimental measurements for different growth configurations [60,94] and by adjusting the effective conductivity of the melt until reasonable agreement between the computed and experimental melt/crystal interface shape is achieved.

This fitting is accomplished by modeling convective transport in the melt using the concept of a thermal boundary layer in the melt, below the interface. This boundary layer forms below the rotating crystal [95], and is modeled to be thicker in the centerline part than at the edge of the crystal, as the rotation speed increases linearly with increasing radius. Hence, the convective heat transport and in turn the effective conductivity are expected to be lower in the center than near the edge of the crystal. The following form of the effective thermal conductivity within the melt (Eq. (3.4)), gives the best fit to the interface shape

$$k_{\text{eff}}(\text{bulk}) = 110 \text{ W/m K}, \quad k_{\text{eff}}(\text{interface}) = k_{\text{eff}}(r) = \left(1 + \frac{r}{R_c}\right) \times 55 \text{ W/m K}, \quad (3.4)$$

where the interfacial region is defined to extend a distance of 30 mm from the interface into the melt, and with a maximum radius equal to the crystal radius R_c . Good agreement between the computed and measured shapes of isotherms in the melt are obtained only if crucible and crystal rotation are applied. This is always the case in silicon crystal growth, where crucible and crystal rotations of several rpm are used. Buoyancy-driven convection alone (i.e. no rotation) tends to generate vertical isotherms [60], resulting in poor agreement with the effective conductivity model.

The validity of the effective conductivity model was tested by considering the interface shapes of 150 mm crystals grown in two different hot zones labeled HZ-I and HZ-II with pull rates of 1.5 and 0.9 mm/min, respectively. In these experiments, HZ-I led to a slower cooled crystal as compared to HZ-II. Hot zone HZ-I generated a completely concave interface with a deflection of 8 mm for the 150 mm crystal grown at a pull rate of 1.5 mm/min (see Fig. 3). Hot zone HZ-II resulted in not only faster cooling of the crystal, but also changed the interface shape from concave to a doubly curved, or ‘gull-wing’ geometry at a pull rate of 0.9 mm/min, also shown in Fig. 3. Measurement uncertainties were in the range of 10%.

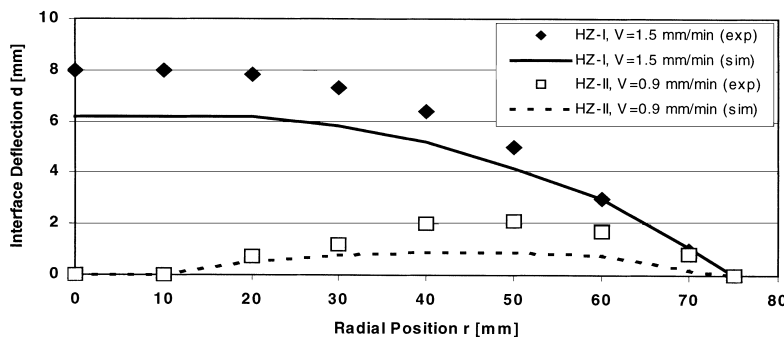


Fig. 3. Comparison between experimental (symbols) and computed (solid and dashed lines) interface shapes for 150 mm crystals grown in hot zone HZ-I with a pull rate of 1.5 mm/min and in hot zone HZ-II with a pull rate of 0.9 mm/min.

The temperature distributions and interface shapes for the test cases were computed by applying the effective conductivity model described by Eq. (3.4). In all cases, the simulation was found to represent the experimental results well, even reproducing the gull-wing shape found in the HZ-II/0.9 mm/min case. Simulation predictions using a constant k_{eff} for the complete melt could not predict doubly curved interfaces for any configuration, and interface shapes were found to be more concave than measured.

For larger melts containing more than 100 kg of silicon, the value of k_{eff} is expected to increase with increasing melt charge as convection becomes more intense. An estimate of the sensitivity of the interface shape on k_{eff} shows that even if k_{eff} is increased to 220 W/m K, the deflection would change by less than 1 mm. Hence, the heat flux balance at the interface and the temperature in the crystal would not be influenced strongly as the heat transfer in the melt is increased. Using an enhanced conductivity for the overall heat transport in CZ silicon melts provides a good compromise with respect to accuracy and computation time. However, more detailed prediction, that is robust to changes in operating conditions and system geometry will have to await use of the coupled simulation of turbulent melt convection and temperature field [63].

3.3.2. Radiative heat transfer

Radiative heat transfer plays an important role in CZ silicon crystal growth, as the maximum temperatures in the furnace are approximately at 1700°C, where natural emission in the infrared wavelength range (0.1–100 μm) is significant. Hence, the temperature of the growing silicon ingots and of furnace components depends strongly on radiative transport. Accurate modeling of radiative heat transfer is essential for quantitative prediction of crystal temperature fields. Analytical approximations, and Monte Carlo and net radiation methods have been applied for solving the radiation heat transfer in enclosures [96]. The net radiation method was chosen for FEMAG, because of its accuracy and computational efficiency. A detailed description of the physics that describe radiative heat transfer and associated numerical methods can be found in [76,77,97], and was developed by Wouters [98], Dupret et al. [76] and van den Bogaert [99] based on the net radiation method described by Howell and Siegel [96]. The main assumptions for the development of the radiation model are that:

1. all material surfaces are diffuse reflectors; specular radiation is neglected;
2. emission, absorption and reflection only occur at surfaces and not within bodies;
3. all surfaces are opaque or fully transparent;
4. the material properties (emissivity) are independent of temperature and wavelength in a given enclosure, within fixed wavelength ranges $\Lambda=[\lambda_i, \lambda_{i+1}]$, i.e. a band energy method is applied. In most cases, the bodies are, however, considered as gray emitters.

The net heat gain q_n of a body by radiation is equal to the difference of incoming flux q_i and outgoing flux q_o , where q_o is the sum of the emitted flux from the surface dS and the reflected part of the incoming flux. The incoming heat flux q_i consists of contributions from all surfaces in the enclosure. Lambert's law for diffuse radiation defines the contribution from each surface by the surface view factor $K(\bar{r}, \bar{r}^*)$, where \bar{r} and \bar{r}^* are the coordinates of two elementary surfaces dS and dS^* with normal vectors \bar{n} and \bar{n}^* . The value of $K(\bar{r}, \bar{r}^*) dS$ is in the interval of [0,1] for surfaces that view each other, and $K(\bar{r}, \bar{r}^*)$ is zero, if they do not view each other (Fig. 4). The incoming flux is calculated as the integral of the outgoing fluxes from all surfaces, weighted with the surface view factors. The view factor calculation in FEMAG includes a quasi-three-dimensional treatment of all bodies in the growth furnace, taking into account viewed and hidden surfaces. Surface temperatures and radiative fluxes are connected through the radiative matrices.

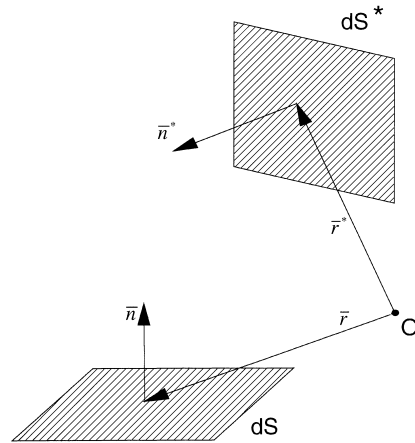


Fig. 4. Surface view factors between two elements viewing each other [76].

3.4. Temperature distribution prediction in CZ crystals

Temperature distributions in two 100 mm crystals were measured with PtRh30/PtRh6 thermocouples (as shown in Fig. 5a) and compared with calculations. Pre-pulled crystals were mounted in an industrial CZ silicon puller (Leybold EKZ 1300) after installing thermocouples in drilled out holes. After heating up to process temperature, the prepared crystals were brought into

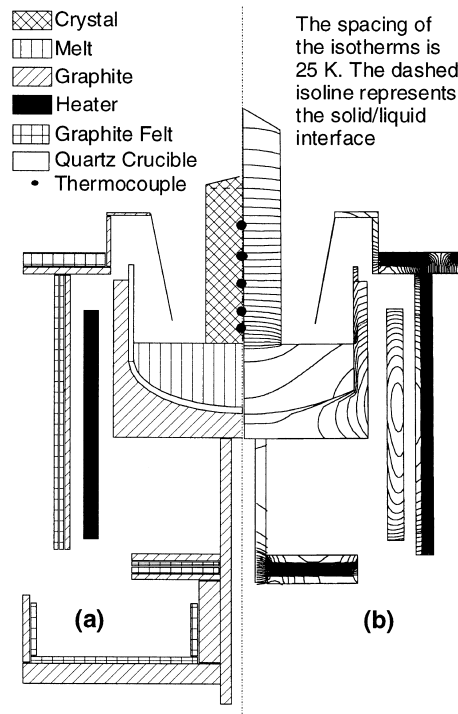


Fig. 5. (a) Schematic drawing of a CZ silicon furnace with heat shield. Thermocouples are installed in a prepulled 100 mm diameter crystal. (b) Calculated global temperature distribution.

contact with a 10 kg silicon melt in a crucible rotating at 5 rpm. The crystal was not rotated because of the thermocouple installation. After re-melting of the crystal/melt contact region a slightly concave crystal/melt phase boundary was established. Because no crystal growth took place, no latent heat was released and the heat flux across the crystal/melt phase boundary was determined solely by the temperature fields in the melt and crystal. The temperature in the crystal was measured after a steady state was established. In a second experiment, a radiation shield was added as sketched schematically in Fig. 5a. This radiation shield was expected to have a large impact on the temperature distribution within the crystal, because the direct radiation from the melt and from the upper heater was partially screened.

The global temperature distribution within the furnace containing the heat shield is shown in Fig. 5b. In this case, a measured heater power of 62 kW was required to maintain thermal equilibrium, as compared to 65.1 kW predicted by the simulation. The difference between the simulation and experimental values may be attributed to the treatment of the melt flow and to uncertainties concerning the heat loss at the water-cooled walls of the CZ system. A heater power of approximately 70 kW was needed for the furnace without the heat shield. Computed and measured power differed in both cases about 5%.

The temperatures along the crystal axis are compared for the furnace setup with and without use of a heat shield in Fig. 6. The difference between measured and simulation values is about 10–15 K. The highest discrepancies are found near the solid/liquid interface. With the heat shield, the axial temperature gradient in the lower part of the crystal (approximately 50 mm above the melt) is about two times the gradient for the case without a heat shield. The temperature along the upper part of the crystal grown with a heat shield is about 200 K lower than for the case without heat shield.

During crystal growth with a pull rate of about 1 mm/min, the agreement between the simulation results and measurements close to the interface should improve because the heat flux at the interface will be influenced by latent heat release which is of the same order of magnitude as the heat flux coming from the melt. At 20–30 mm from the interface, the temperature along the crystal axis becomes independent of the heat flux conditions in the melt. The thermal history of a crystal is, therefore, predominantly determined by radiative heat transfer and conduction, which is clearly demonstrated by the influence of the radiation shield.

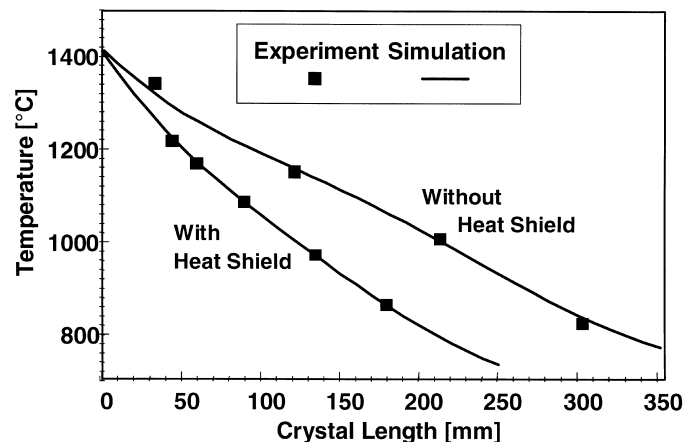


Fig. 6. Computed and measured temperatures in crystals grown with and without heat shield. Crystal length 0 mm corresponds to the solid/liquid interface.

3.5. Conclusions

The results discussed in this section clearly demonstrate that numerical models are available today for the calculation of the temperature distribution in Czochralski silicon crystals. These models can predict the temperature distribution in a growing silicon crystal, which is important for the optimization of growth processes and the engineering of grown-in microdefects. The heat transfer model described in Section 3 was used to compute thermal fields and melt/solid interface shapes for all subsequent microdefect dynamics simulations discussed. These calculations are now discussed in detail in the remaining Sections.

4. The OSF-ring

One of the most frequently studied microdefect structures in silicon is the ring-like distribution of OSFs that appear after wet oxidation of wafers grown by the Czochralski method (CZ). The OSF-ring is seen at a radius that depends exclusively on the growth conditions [100,101], namely the temperature field in the crystal and the growth rate; a typical example of OSF-ring response to growth rate is shown in Fig. 7. The OSF-ring has received much attention because it offers a unique opportunity for application of the modern materials engineering mantra, ‘multiscale simulation’. In particular, its structure allows for a very clear separation of length scales where information obtained at the atomic scale can be used directly in continuum scale calculations.

Numerous studies indicate that the microdefects which lie inside the ring region are formed by vacancies while those that lie outside the ring are self-interstitial in nature. In other words, the OSF-ring can be regarded as a visible boundary between two regions, each dominated by one of the two native point defect species. This observation provides a link between the location of the OSF-ring and the point defect distribution pattern within a crystal grown by the CZ method.

Clearly, the microdefect species that exist in the two regions (either self-interstitial or vacancy dominated) are very different in nature. Most current CZ growth processes are tailored so that the OSF-ring region is located at the edge of the wafer, leading to a completely vacancy dominated

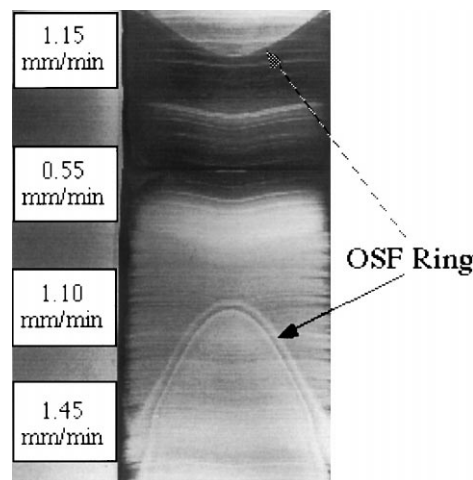


Fig. 7. Oxidation-induced stacking fault ring (OSF-ring) response to changes in the crystal growth rate.

crystal. There is much demand for simple quantitative models that predict these defect structures and their dependence on the temperature field in the crystal and pull rate. This simplicity can be obtained if the details of point defect aggregation can be ignored. This goal has been achieved for prediction of the OSF-ring where only point defects are needed to characterize its radial location. Detailed analysis of aggregation phenomena is described in Sections 4.2 and 4.5.

4.1. Experimental characterization of the OSF-ring

The OSF-ring has been studied extensively using experiments designed to characterize quantitatively its behavior as a function of crystal growth operating conditions. Studies by Abe et al. [102,103], Hasebe et al. [101], and Dornberger et al. [104] found that the radius of the OSF-ring depended exclusively on the crystal growth conditions and not the subsequent thermo-chemical annealing, even though the OSF-ring was not visible with X-ray topography until after thermal oxidation of the wafer. Transmission electron microscopy (TEM) has shown that the OSF-ring contains extrinsic (interstitial-type) stacking fault loops lying on $\langle 111 \rangle$ crystallographic planes that grow isotropically from nuclei containing oxygen [105], which are postulated to be SiO_X precipitates, where $1 \leq X \leq 2$. These studies led to the conclusion that oxygen precipitates are first formed during CZ growth which then provide the nuclei for interstitial aggregation in stacking faults during the steam oxidation of the wafers. Steam oxidation of silicon wafers is known to result in the formation of an SiO_2 surface on the wafer, which acts as a source of self-interstitials injected into the bulk through a strain releasing mechanism [101].

Recent experimental investigations have characterized the dependence of the radial location of the ring with respect to changes in the crystal pull rate and the crystal temperature in a CZ system [104]. The temperature field in the crystal for several heat transfer packages and values of the pull rate were computed using the numerical simulations described in Section 3. A major result of these studies was that the location of the OSF-ring, $r=R_{\text{OSF}}$, correlates very well with a constant value for the ratio of the pull rate (V) to the interfacial axial temperature gradient at the melt/crystal interface, $G(R_{\text{OSF}})$. This value, $(V/G)_{R_{\text{OSF}}} = 1.34 \times 10^{-3} \text{ cm}^2/\text{min K}$, referred to as the critical value, was observed to be constant for 4–8 in. diameter crystals across a range of pull rates and heat transfer configurations, as shown in Fig. 8. Here, the four hot zones are listed as HS1–HS4, where HS1 cools the crystal slowest and HS4 fastest.

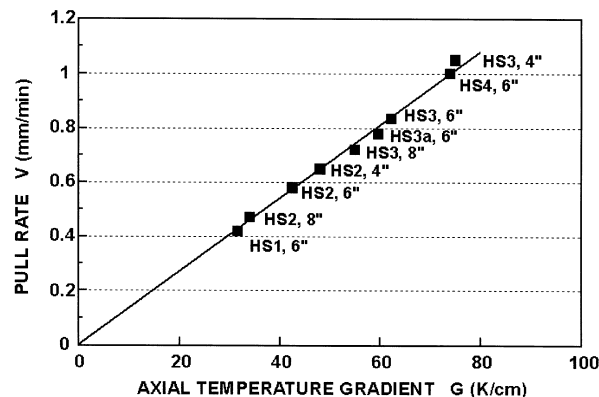


Fig. 8. Critical pull rate (v_{crit}) as a function of the computed axial temperature gradient G at the melt/solid interface.

4.2. Point defect connection to the OSF-ring and the model of Voronkov

The opportunity for quantitative modeling and prediction of such a clearly defined microdefect has led several investigators to attempt to use point defect dynamic properties to develop continuum-scale models aimed at the location of the OSF-ring [12,21–23]. Although direct experimental observations are typically limited to microdefects of size 50 nm or larger, it is now believed that the critical step in differentiating between self-interstitial and vacancy type microdefects is the presence of a dominant point defect species, which exists in supersaturation relative to the local thermodynamic conditions. This connection is based on the hypothesis that microdefects from either point defect type grow at rates that are proportional to the driving force for point defect aggregation due to supersaturation of the surrounding bulk crystal. This picture was first used in a semi-quantitative analysis by Voronkov [106] in order to describe the dynamics of A-defect (also known as ‘swirl defects’ because of their striated distribution) and D-defect distributions in crystals grown by the floating zone technique. We describe this model in some detail below because it represents a unifying theme for more recent work aimed at predicting the dynamics of the OSF-ring in CZ silicon, but first we give a brief review of microdefect formation in FZ silicon.

The primary advantage of FZ silicon from a microdefect modeling point of view is the relatively low concentration of interstitial oxygen which generally leads to a simpler microdefect profile. Early observations focused on the striated defects (A-defects) observed for certain growth conditions. Speculation on their composition was based on the prevailing preference for either self-interstitials or vacancies. Initially it was assumed that, in analogy to the situation in metals, vacancies were the dominant species, and therefore all defect species, including swirls, were vacancy related [107]. Later TEM studies showed that in fact self-interstitial aggregation was more likely to be the cause of these defects [108]. The opposite response of D-defects to crystal growth operating conditions led to the conclusions that they were of vacancy origin [109]. These observations led to a large number of proposed semi-qualitative models for the formation of microdefects in FZ silicon based on homogeneous and heterogeneous nucleation mechanisms [110]; see Sinno [13] for a review of these models.

However, it was not until the model of Voronkov [106] that a detailed quantitative analysis of point defect dynamics was connected to the observed distributions of microdefects. It is now established that during crystal growth, point defects are incorporated into the silicon lattice across the rapidly moving melt/solid interface. In addition to the convection of point defects by crystal translation, they are also transported by diffusion. As the crystal cools, the equilibrium concentration of point defects is reduced exponentially with temperature, creating a strong driving force for point defect annihilation by the reversible recombination reaction described in Section 2. This process can continue until one of the two point defect species is exhausted, leaving behind a continuously increasing supersaturation of the remaining species. This supersaturation then leads to the formation of related microdefects if diffusion to the crystal surface is insufficient for dissipating the excess concentration. A key element to this picture is the fact that both diffusive transport and any reactions, including aggregation, are effectively extinguished at low temperature, leaving behind a ‘frozen-in’ microdefect concentration, which can subsequently be imaged experimentally.

According to this interpretation, Voronkov defined a quantity $\Delta(r)$ in the cold upper portion of the crystal where the point defect profiles are no longer changing axially

$$\Delta(r) = C_I(r) - C_V(r). \quad (4.1)$$

Thus, the tendency for self-interstitial type microdefects to dominate corresponds to $\Delta > 0$, while

vacancy microdefects correspond to regions where $\Delta < 0$. There exists significant evidence that such a model is also qualitatively accurate for the case of CZ-grown silicon and the OSF-ring. The region inside the OSF-ring has been shown to contain vacancy rich microdefects while the region outside the ring typically consists of interstitial based microdefects. The radial distribution of these microdefects is qualitatively similar to microdefect distributions observed in floating-zone (FZ) crystals, and the dynamic behavior of the OSF-ring position is qualitatively identical to the defect-free region between A-defects and D-defects observed in FZ material [103], known as the ‘neutral zone’. In fact, this apparent similarity, despite radically different oxygen and impurity profiles in the two materials is strong evidence for a point defect dominated mechanism for dynamics.

The fact that an OSF-ring is not apparent in FZ material is an outstanding problem. Experiments where FZ crystals are doped with oxygen at levels similar to those of CZ crystals have been performed [111], however, despite using similar oxygen concentrations, oxygen-doped FZ (OFZ) crystals do not show an OSF-ring at the location of the neutral zone. One explanation is that the appearance of the OSF-ring is a function of oxygen and other variables, most likely the cooling rate of the growing crystal at lower temperatures. OFZ crystals are grown at much higher cooling rates than the large diameter CZ crystals and this could lead to insufficient time for stacking fault nuclei to develop. Fortunately, we do not require an understanding of the details of the nucleation process in order to consider the dynamics of the OSF-ring.

The simple picture put forth by Voronkov above suggests that microdefect growth is essentially controlled by the dynamics of intrinsic point defects in the crystal. If we accept that both the neutral zone in FZ crystals and the OSF-ring region share the same dynamics, then the OSF-ring location, denoted by $r = R_{\text{OSF}}$, would correspond to $\Delta \sim 0$ or

$$\Delta(r = R_{\text{OSF}}) \approx 0. \quad (4.2)$$

This interpretation of microdefect dynamics was applied by Voronkov to FZ microdefect dynamics through the consideration of point defect fluxes entering the crystal by convection and diffusion in one dimension. The model was able to describe successfully the macroscopic distribution of microdefects as a function of crystal growth rate for physically reasonable thermophysical property estimates for self-interstitials and vacancies. Previous experimental work has shown that the growth conditions at which A-defects disappear from an FZ crystal [31,102] are related to a constant value for the ratio of V/G . These observations are very similar in nature to the results of Dornberger et al. [104] described above and give confidence in the hypothesis that intrinsic point defects control the dynamics in both cases. By comparing the results of his analysis to experiments, Voronkov established rough estimates for the point defect properties, and a reasonably good estimate for the value of V/G that corresponds to the transition between A-, B- and D-defects.

The limitation of Voronkov’s original analysis stemmed from the reliance on the assumption that a one-dimensional model is capable of predicting the radial distribution of microdefects. By not considering a two-dimensional thermal environment, the model required a separate treatment of the radial problem in which the cylindrical surface of the crystal was assumed to act as a sink for point defects. While this mechanism is indeed significant near the crystal surface, the radial variation of the crystal thermal field was neglected and, as discussed below, is now known to be the major component in controlling OSF-ring and neutral zone dynamics.

It is worth mentioning a refinement to the above model for the OSF-ring position. It is now well known that the OSF-ring in fact appears just inside the self-interstitial/vacancy (IV) boundary across most of the crystal radius and diverges significantly from the $\Delta = 0$ contour near the surface of the crystal [112]. In the crystal interior, the error incurred in assuming that the OSF-ring lies on the

$\Delta=0$ contour is well within the uncertainty in the model parameters. The situation is different near the crystal surface where diffusion of point defects to the surface leads to qualitatively different behavior. This behavior can be understood in terms of vacancy mediated oxide precipitation which is discussed briefly in Section 5. We note here that our model described in Section 4 does not take this into account and therefore is accurate only in the interior portions of the crystal and not near the cylindrical surface.

4.3. Quantitative models for point defect dynamics

All modeling efforts aimed at the prediction of OSF-ring (or neutral zone) dynamics are based on the point defect balance equations described in Section 2.2.1. The main difference in these approaches is the choice of thermophysical property estimates for the point defects, the boundary conditions imposed at the crystal surface. The former is particularly significant because the uncertainty in these parameters, coupled with the sensitivity of Eqs. (2.15)–(2.25) to them, has led to greatly varying results and interpretations. We present here a brief summary of previous efforts.

One of the first detailed analyses of OSF-ring dynamics was performed by Habu and coworkers [22,113,114]. They used a similar form of Eqs. (2.15)–(2.25) to generate a set of conditions which led to qualitatively correct predictions of the OSF-ring response to the crystal growth rate but not to the radial variations in the thermal field. The predicted dynamical response to radial thermal gradients was interpreted in the context of a thermodiffusion effect [20], which was large enough to lead to so-called ‘uphill diffusion’ where the net flux of point defects was toward the melt/crystal interface despite the concentration gradient driving force in the opposite direction. It has been shown that the values for the point defect properties necessary to make this model predict quantitatively the OSF-ring positions are somewhat at odds with accepted measurements and other estimates. Furthermore, the Habu model correlates the position of the OSF-ring with a peak in the self-interstitial concentration rather than the vicinity where self-interstitials and vacancies are in approximate balance.

Others have also solved numerically the point defect balance equations in an attempt to describe microdefect formation, and in particular the IV boundary. Wijaranakula [21] additionally considered the effects of thermal stresses and charge distribution on the point defect profiles. In these calculations, the thermal gradients were estimated using an approximate analytical model, and point defect thermophysical properties were obtained from the literature. While the model predicts general trends, such as increasing vacancy dominance with increasing pull rate, there is no evidence for quantitative prediction of OSF-ring dynamics. Tiller et al. [23] also have conducted an analysis of the coupled IV system during crystal growth using a one-dimensional model that accounts for point defect charge states using an effective approach. Neutral point defect thermophysical properties are estimated using atomistic simulations and a linear approximation for the temperature gradient is used for the calculations. The results are in qualitative agreement with other studies but there are no indications that the specified thermophysical properties can reproduce the details of OSF-ring/neutral zone dynamics. Recently, Ebe [115] has reviewed these various approaches and derived qualitative bounds on the point defect thermophysical properties for different mechanistic models involving thermodiffusion.

4.4. Detailed prediction of OSF-ring dynamics

We have developed a quantitative modeling framework based on the numerical solution of Eqs. (2.15)–(2.25) that is based on a self-consistent set of point defect thermophysical properties.

The model is described in detail in Sinno et al. [12]. The position of the OSF-ring is approximated based on Eq. (4.2). Eqs. (2.15)–(2.25) are solved subject to equilibrium conditions at the melt/solid interface (Eq. (2.26)), and no-flux conditions at the surface, which corresponds to setting $K=0$ and $g=0$ in Eq. (2.27). While this assumption is clearly inaccurate in the vicinity of the crystal surface, it has little effect on the point defect distributions, and hence the predicted OSF-ring position, further into the bulk of the crystal. The equations are solved according to the methods described in Section 2.5.

Thermophysical property estimation is carried out using a hybrid approach. The Stillinger–Weber interatomic potential is used to compute the energies of formation and migration for the equilibrium concentrations and diffusion coefficients, respectively. While such calculations are known to have a high degree of uncertainty, our estimates for the activation energy barriers for these properties are well within accepted ranges. The entropies associated with transport and equilibrium are far more difficult to compute. These are yet to be estimated reliably with atomistic simulation. Empirical potential based calculations are not accurate enough, while more detailed electronic structure calculations are too computationally intensive. Instead, we allow the entropic components (D_0 and S^f for I and V) to be varied so that a single set of data for the OSF-ring position as a function of pull rate is reproduced quantitatively. The thermal field and crystal geometry for the simulation are provided self-consistently as input from calculations as described in Section 3. Details of the actual fitting procedure are given in Sinno et al. [12].

Fig. 9 shows the experimental data and simulation results for the fitted case (HS1/4'') as well as two other predicted cases (HS1/6'' and HS2/8'') for different crystal radii and thermal configurations. In all three cases, the model is able to predict well the position of the OSF-ring as a function of the pull rate. Also in Fig. 9 the predicted OSF-ring position according to the empirically derived V/G condition, described in Section 4.1 is shown, which also represents the experimental OSF-ring position well across a wide range of operating conditions.

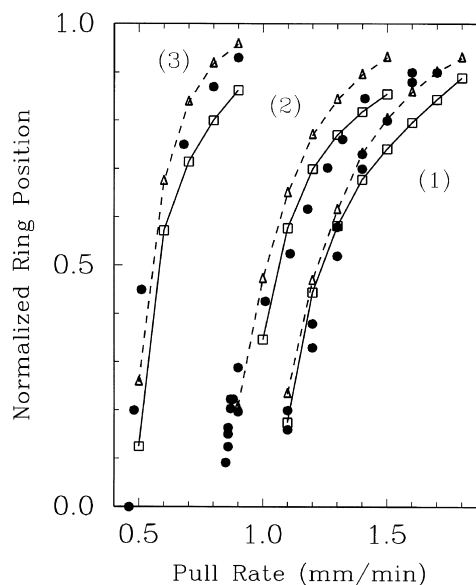


Fig. 9. OSF-ring response to changes in crystal growth rate: (1) HS1/4'', (2) HS1/6'', (3) HS2/8''; \square : simulation results; \triangle : correlation for $(V/G)_{\text{crit}}=1.34 \times 10^{-3} \text{ cm}^2/\text{min K}$; \bullet : experimental results.

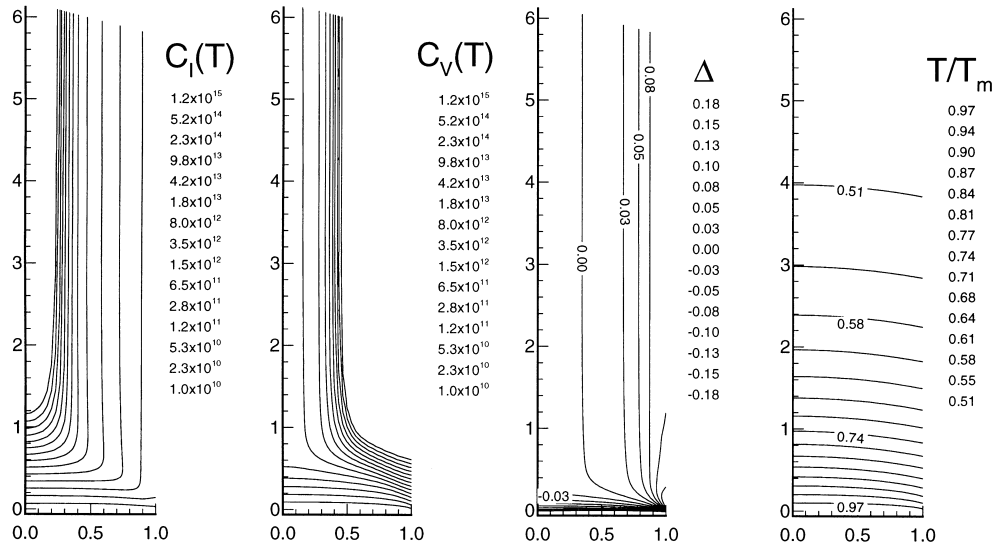


Fig. 10. Profiles for C_I , C_V , Δ and T for the case HS1/6 in. at a pull rate of 1.0 mm/min. Axial and radial coordinates are scaled with the radius of the crystal.

4.4.1. Analysis of the point defect model for OSF-ring dynamics

The fact that the model described here is capable of quantitatively reproducing OSF-ring dynamics without a radial transport driving force (no-flux conditions are imposed on the boundary in the above calculations) suggests that the radial variation in the thermal field is sufficient to explain OSF-ring dynamics, as would also be expected from the apparent success of the empirical V/G model. In order to further understand the details of I and V dynamics during crystal growth it is useful to consider not only the $\Delta=0$ location but the full two-dimensional point defect distribution. The temperature field, self-interstitial and vacancy concentration fields, and contours of $\Delta(r, z)$ are shown in Fig. 10 for a calculation with system HS1 and a 6 in. diameter crystal grown at a rate of 1.0 mm/min.

The general characteristics of these results are typical for point defect dynamics in silicon. First, C_I and C_V decrease rapidly with axial distance from the melt/crystal interface because recombination is rapid. At axial distances greater than one radius, one of the two defect species is exhausted and the concentration of the remaining point defect (I for radii greater than $\sim 0.7R$, V for the rest of the crystal) cannot be reduced further. This species gradually becomes supersaturated as its equilibrium concentration drops exponentially with decreasing temperature. The axial evolution of $\Delta(r, z)$ contours shows the same behavior in that there is no more axial variation once one of the species has been depleted. It is worthwhile noting once again that all radial structure in these profiles appears *exclusively* due to the radial variation in the axial thermal gradient. The qualitative mechanism for the switch between interstitial and vacancy dominated regions is described in detail in Sinno et al. [12]. The salient point is that the total presence of each point defect species at a given radial position is due to the sum of convective and diffusive axial fluxes at the same radial position. Thus, for large growth rates, the convection dominates, favoring vacancies, which are incorporated at higher concentrations, while at small pull rates, interstitials, which diffuse faster, compensate with a larger diffusive flux and therefore establish an excess concentration. In both cases, the driving force for rapid recombination is supplied by the decreasing equilibrium concentrations with temperature.

This mechanism has been explored in detail using an asymptotic analysis of Eqs. (2.15)–(2.25) in the region of the melt/crystal interface. The analysis is justified by the sharp, axial boundary-layer

in the point defect concentrations near the melt/crystal interface which allows for approximations to the full solution to be developed in this regions based on a combination of high-reaction rate and high activation energy asymptotics [12,13]. The major result of the analysis is a closed form expression for $V/G(r=R_{\text{OSF}})$ in terms of the point defect properties at the melting temperature:

$$\left(\frac{V}{G}\right)_{R_{\text{OSF}}} = \frac{D_{\text{I}}(T_{\text{m}})C_{\text{I}}^{\text{eq}}(T_{\text{m}})\gamma_{\text{I}}^{*'} - D_{\text{V}}(T_{\text{m}})C_{\text{V}}^{\text{eq}}(T_{\text{m}})\gamma_{\text{V}}^{*'}}{T_{\text{m}}[C_{\text{V}}^{\text{eq}}(T_{\text{m}}) - C_{\text{I}}^{\text{eq}}(T_{\text{m}})]} \approx 1.38 \times 10^{-3} \text{ cm}^2/\text{min K}, \quad (4.3)$$

where $\gamma_{\text{I,V}}^{*'}$ is a dimensionless effective formation enthalpy of I and V computed from the approximate asymptotic solution of Eqs. (2.15) and (2.16) in the region immediately adjacent to the melt/solid interface. The effective formation enthalpies in Eq. (4.3) are defined as $\gamma_{\text{I,V}}^{*' \equiv H_{\text{I,V}}^{f'}/kT}$ where the prime notation is used to denote that these formation energies are derived from the asymptotic analysis in [12] and contain implicitly thermal field information, and thus are not natural thermophysical properties. The value shown in Eq. (4.3) is in excellent agreement with the empirical value and demonstrates the robustness of the overall model of I and V dynamics for explaining the behavior of the OSF-ring.

The fact that the result of Eq. (4.3) varies to an extent that leads to changes in the surviving point defect concentration for small changes in pull rate and axial thermal gradient is a direct consequence of the unique balance between the self-interstitial and vacancy properties in silicon. In order for Eq. (4.3) to generate the experimentally observed dynamics, the equilibrium concentrations of self-interstitials and vacancies must be within 20–30% of each other, with the vacancy concentration necessarily being the higher value near the melting point. The relative constraint on the diffusion coefficients is weaker, but requires that the self-interstitial diffusion coefficient be higher than the vacancy value at high temperature. A detailed sensitivity analysis of the predicted OSF-ring position with respect to these parameters is presented in [13].

4.5. Thermophysical property estimation

The critical importance of accurate estimates for the point defect thermophysical properties in point defect dynamics models warrants further discussion of our values in the context of other published estimates. Values of the equilibrium concentrations and diffusion coefficients used in these calculations are shown in Figs. 11 and 12 and compared to a representative sample of other estimates, obtained from both simulation and experiment. While our current estimates lie comfortably within the range outlined by other investigations, the uncertainty is clearly large enough to render a direct comparison of individual properties meaningless.

Discrepancies between thermophysical property estimates derived from metal diffusion and OED/ORD experiments have been discussed by Agrawal and Dunham [116] in terms of surface segregation coefficients. This issue serves to highlight the fact that individual thermophysical properties of point defects cannot be directly measured.

A more informative comparison is to the self-diffusion contributions for self-interstitials and vacancies. The self-diffusion coefficient for each species is defined as the product of the diffusivity and equilibrium concentration, i.e. $D_{\text{I}}C_{\text{I}}^{\text{eq}}$ and $D_{\text{V}}C_{\text{V}}^{\text{eq}}$ for self-interstitials and vacancies, respectively. These quantities can be estimated from experiment far more directly and the literature estimates show much less scatter, as demonstrated in Fig. 13.

Our values for the self-diffusion coefficients are in very good agreement with measured values, particularly near the melting temperature. It is important to note that a key aspect of our results is that the OSF-ring is a function only of point defect properties very near the melt/solid interface,

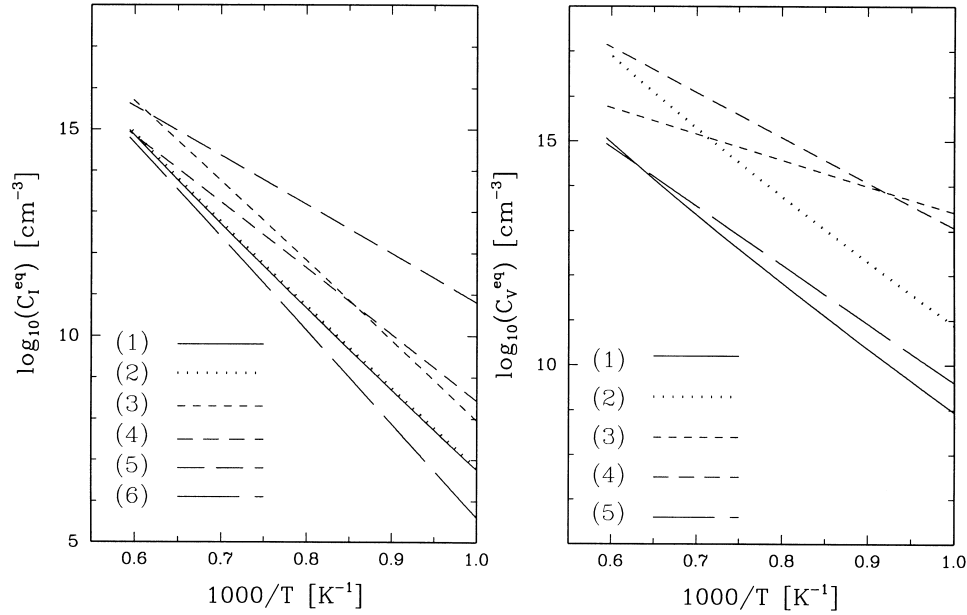


Fig. 11. Equilibrium concentrations for (a) self-interstitials and (b) vacancies from the OSF-ring model in this work compared to other literature estimates. a: (1) this work, (2) unadjusted Stillinger–Weber results, (3) gold diffusion data [29], (4) zinc diffusion data [32], (5) OED/ORD experiments, and (6) Habu OSF-ring model [22]. b: (1) this work, (2) unadjusted Stillinger–Weber results, (3) gold diffusion data [29], (4) zinc diffusion data [32], and (5) Habu OSF-ring model [22].

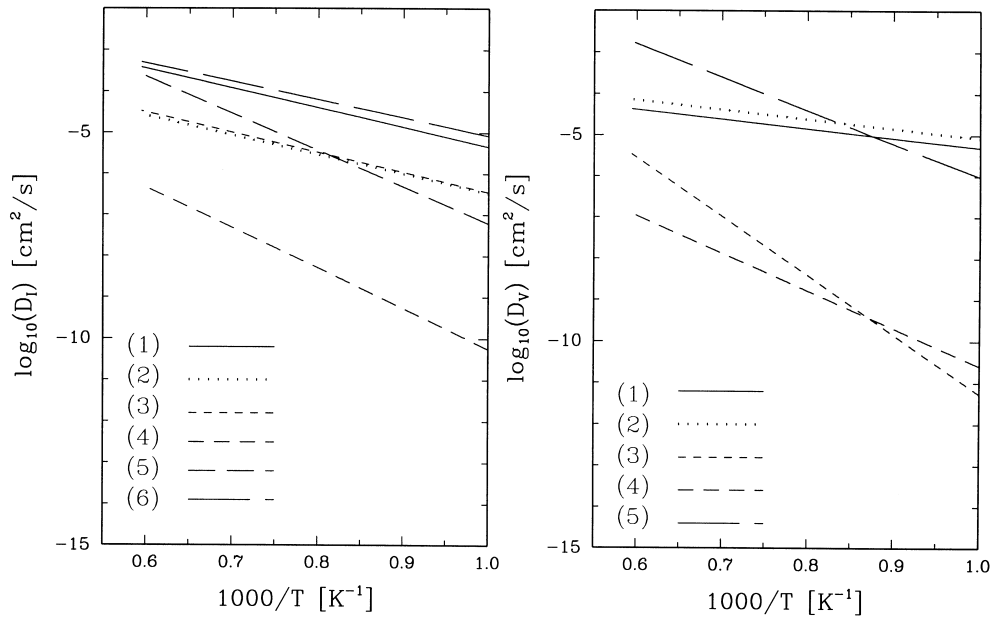


Fig. 12. Diffusion coefficients for (a) self-interstitials and (b) vacancies from the OSF-ring model in this work compared to other literature estimates. a: (1) this work, (2) unadjusted Stillinger–Weber results, (3) gold diffusion data [29], (4) OED/ORD experiments, (5) zinc diffusion data [32], and (6) Habu OSF-ring model [22]. b: (1) this work, (2) unadjusted Stillinger–Weber results, (3) gold diffusion data [29], (4) zinc diffusion data [32], and (5) Habu OSF-ring model [22].

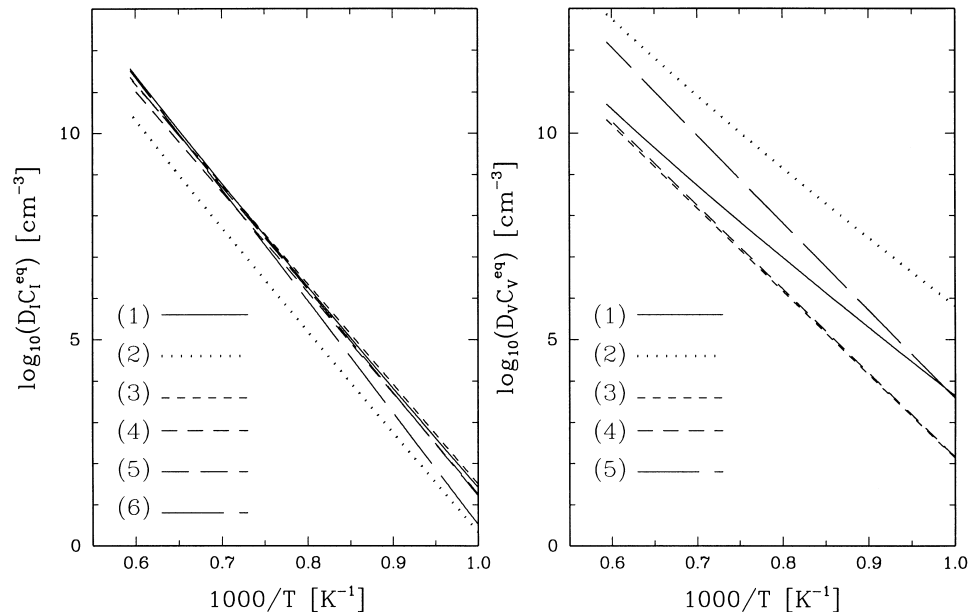


Fig. 13. Self-diffusion coefficients for (a) self-interstitials and (b) vacancies from the OSF-ring model in this work compared to other literature estimates. a: (1) this work, (2) unadjusted Stillinger–Weber results [39], (3) gold diffusion data [29], (4) zinc diffusion data [32], and (5) Habu OSF-ring model [22]. b: (1) this work, (2) unadjusted Stillinger–Weber results, (3) gold diffusion data [29], (4) zinc diffusion data [117], and (5) Habu OSF-ring model [22].

which implies an insensitivity to low temperature properties and thus the energies of formation. The deviation from the literature estimates is particularly noticeable for the vacancy, and is explained by the relatively low accuracy of the SW potential in this case.

The self-diffusion coefficients predicted entirely by the atomistic simulations also are shown in Fig. 13. While the results are quite good for the self-interstitial point defect, there is significant deviation across the entire temperature range for the vacancy, further highlighting the inadequacy of the SW potential for computing vacancy entropic properties. Better estimates for the vacancy formation enthalpy will be required to preserve the robustness of our modeling effects, particularly if lower temperature phenomena, such as precipitate growth, are to be predicted with a single set of point defect thermophysical properties.

4.6. Simulation of microdefect distributions

The point defect dynamics model described in this section has been shown to explain and predict quantitatively the dynamics of the OSF-ring. However, current simulation efforts are aimed at understanding quantitatively the distribution of microdefects found in each of the regions described here. This is a far more complex task because most microdefects tend to be highly geometrically and chemically heterogeneous structures, often nucleated by the presence of impurities, typically oxygen. A notable exception to this rule are voids, which are now known to consist of a condensed phase of vacancies, or more simply put, empty space arranged in an octahedral geometry. The fact that all commercial CZ silicon is grown under vacancy rich conditions which generally lead to void formation during growth and processing, and that these voids are known to be harmful to device performance has spurred intense efforts aimed at extending the capabilities of OSF-ring models to allow for an explicit representation of aggregation processes. Almost all such investigations are

based on the diffusion-limited homogeneous nucleation theory outlined in Section 2. The applications of this theory, as well as a detailed characterization of the nature of voids will be discussed next.

Before discussing aggregation in detail, however, it is informative to consider further any information that can be gleaned from the simple point defect dynamics model described here. An important prediction of the model is the final vacancy concentration inside of the defect neutral region, $\Delta \sim 0$. Characteristic values of $C_V(r, L)$ (L represents the top of the crystal) are on the order of about 10^{13} – 10^{14} vacancies per cubic centimeter inside the OSF-ring for the point defect properties used in our study. This concentration of vacancies would be available to aggregate into the voids that are observed experimentally, if it is assumed that most void nucleation and growth takes place after point defect recombination is complete. This order-of-magnitude estimate is in fact very much in line with measurements of void size and density observed in commercial crystals [118].

The discussion in the following Section deals explicitly with the prediction of void formation and demonstrates that the above assumptions of sequential processes do in fact occur. This provides somewhat of an a posteriori verification for our preceding analysis, which implicitly neglected the effect of nucleation and aggregate growth in the region near the melt/solid interface. This fortuitous set of circumstances leads to an important separation of problems that allows us to reduce the number of parameters that must be considered simultaneously within the microdefect dynamics model.

5. Vacancy aggregation

5.1. Characterization of grown-in defects in vacancy-rich crystals

A summary on the characterization of vacancy related grown-in defects, and a discussion on the impact of these defects on device yield is relevant to the modeling presented below. Most CZ silicon crystals are grown under vacancy-rich conditions, if the OSF-ring is located at the crystal rim. Itsumi and coworkers [119–121] and Park and coworkers [122,123] have demonstrated that grown-in defects in vacancy-rich crystals are octahedral voids of about 100–300 nm in diameter and proposed that these voids are agglomerates of vacancies. Grown-in voids have been studied extensively, because polished wafers for device manufacturing are made predominantly from such vacancy-rich crystals.

Voids exhibit deleterious effects on device performance such as gate oxide breakdown as well as enhanced leakage current if they are located near the wafer surface [122,123]. Grown-in defects in vacancy-rich crystals are frequently termed D-defects by analogy to the defects seen in FZ crystals. A litany of other names have also been used, depending on the characterization technique used to elucidate their presence; examples are flow pattern defects (FPDs) [124], crystal originated pits (COPs) [125] and light scattering tomography defects (LSTDs) [126]. More recently, TEM [119] and atomic force microscopy (AFM) [127] have been used to identify the shape and size of these defects. The chemical composition of these defects has also been examined by energy dispersive X-ray spectroscopy (EDX) methods [119]. We briefly outline some of these investigations because voids are one of the most important technological issues in CZ crystal growth today.

5.1.1. Transmission electron microscopy (TEM)

Itsumi and coworkers [119,120] observed octahedral voids with typical sizes of about 200 nm by TEM (Fig. 14, source [128]). The voids typically appear in densities too low to be found directly

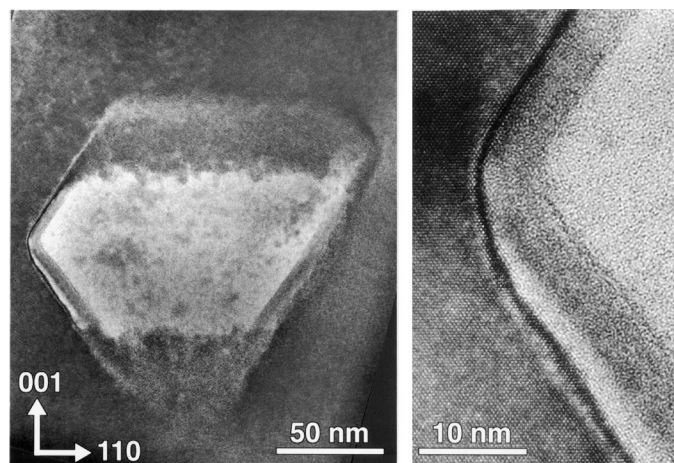


Fig. 14. Octahedral void (a) with a thin amorphous oxide layer at its surface (b) in an as-grown CZ silicon crystal [128].

with TEM, copper decoration was first used to highlight the defects, followed by marking with a focused ion beam (FIB). After removal of the copper decoration and etching, voids were imaged directly with TEM. An interesting, and yet unexplained phenomenon observed in these studies is the appearance of double or even triple void [129] arrangements. The faces of the octahedral voids were seen to be oriented along the high-index (1 1 1) direction, and covered with a 2 nm amorphous layer. Subsequent EDX measurements have detected weak oxygen signals, suggesting that the defects are agglomerates of vacancies with a thin oxide layer.

5.1.2. Flow pattern and Secco etch defects

The delineation of vacancy related defects as FPDs was developed by Yamagishi and coworkers [124,130] and is an efficient method for the characterization of as-grown crystals. Here, wafers are prepared for FPD testing by HF/HNO₃ etching. The wafers are then placed vertically into a non-agitated Secco etchant for about 30 min, resulting in a removal of a 30 μm silicon layer. The etching process corrodes small pits into the wafer surface at the nuclei of the FPDs. Chemical reaction of the Secco etch with the defect produces hydrogen bubbles [131], which are driven upward by buoyancy. Part of the wafer is covered and protected from further corrosion by the hydrogen gas. In the course of the upward flow, the gas layer becomes wider and generates the typical wedge shaped flow pattern with a deeper etch pit at the nucleus (Fig. 15). The expression FPD has been derived from the wedge shaped flow patterns. FPD densities are counted by using optical microscopes.

Further etching results in further Si removal and corrodes flow pattern nuclei in deeper layers. As the existing defects are conserved, the final FPD density on a wafer is directly related to a FPD volumetric concentration. SEPs are etch pits that appear without wedge shaped flow patterns. Takeno et al. [132] have suggested that both FPDs and SEPs are nucleated by mechanisms other than simple aggregation of vacancies. FPDs and SEPs are observed typically with densities of 10⁴–10⁵ cm⁻³ in vacancy-rich silicon.

5.1.3. Characterization of voids as crystal originated particles (COPs)

Ryuta and coworkers [125,133,134] were the first to report COPs. This term was assigned to observed singularities of about 100–300 nm in size [135], revealed as shallow pits by repetitive SC1 treatment of polished wafers [136]. Effective diameter data was obtained by calibration of laser counters using latex microspheres of known diameter [137]. Atomic force microscopy (AFM)

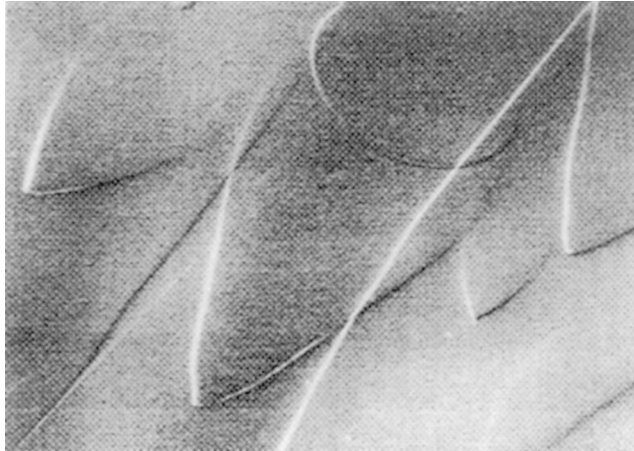


Fig. 15. Wedge-shaped FPDs on a silicon wafer.

revealed that a COP etch pit is pyramid-shaped with a rectangular basis on a $\langle 100 \rangle$ surface and with a hexagonal basis on a $\langle 111 \rangle$ surface (see Fig. 16) [127]. Taking into account that the upper part of a COP would have been removed by polishing and etching, the complete defect would be octahedral in shape with faces along the $\{111\}$ direction. Dual and even triple COP etch pits are frequently observed. However, a conclusive explanation is still missing for the formation of multiple COPs. These observations are in accordance with the TEM observations described above.

5.1.4. Light scattering tomography defects

Infra red light scattering tomography (IR-LST) is a non-invasive technique that can be used to scan relatively large volumes of a wafer [138–142]. Bulk defects in the wafer scatter light from a Nd-YAG laser beam, which is collected under an angle of 90° by an infrared camera. An example of the use of this technique is the study of Kissinger and coworkers [143,144]. The detection limit for this

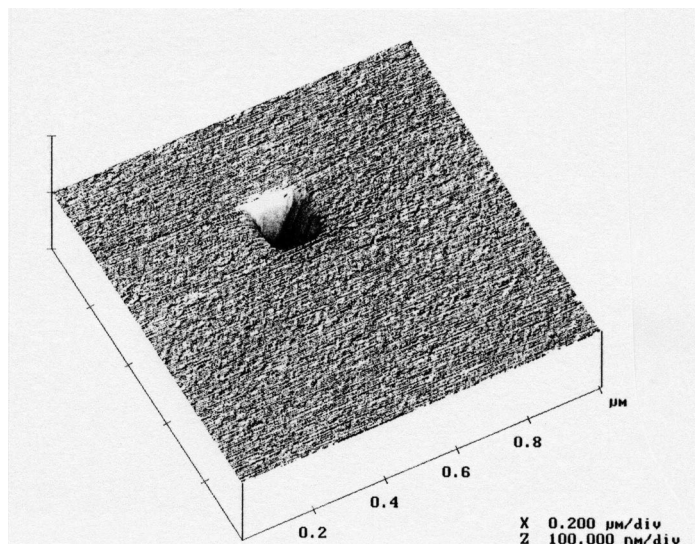


Fig. 16. AFM image of a COP after SC1 cleaning [127].

technique is a defect density of about $2 \times 10^5 \text{ cm}^{-3}$ per scan. Several tens of defect counts are detected per scan in this mode of operation leading to measured defect densities of $O(10^6\text{--}10^7 \text{ cm}^{-3})$. Information on the size distribution for LSTDs also is obtained with this technique because the radius of the light scattering object is proportional to the sixth root of the scattering intensity.

5.2. *Impact of vacancy-type defects on gate-oxide integrity*

Perhaps the best known feature of vacancy-type defects is their effect on the gate oxide integrity (GOI). Gate oxide integrity (GOI) testing is a standard method used to determine the electrical quality of wafers [145–149]. After describing the GOI test procedure, the impact of defects in the vacancy-rich area on the GOI yield and on the yield in device manufacturing is discussed below. The quality of the gate oxide correlates with DRAM reliability and device failure rates, making it one of the key parameters in device yield estimation [146]. Voltage breakdown on substrate wafers has, besides grown-in vacancy defects, several other origins, such as metallic impurities [150–152] (e.g. Cu, Fe and Na), doping conditions, surface roughness [153–155], wafer warpage [156], and oxygen content [157]. In addition, numerous other sources for gate oxide degradation can crop up during device manufacturing [145]; e.g. metal contamination or plasma damage caused by various plasma processes [158].

The time zero dielectric breakdown GOI yield (TZDB) of substrate wafers is tested by depositing poly-silicon capacitors on the gate oxide and applying a voltage or a current until the capacitor fails. Frequently, the E_{bd} -test is used, where a constant or a ramped voltage is applied to the capacitors and the current is measured [145]. Gate oxide breakdown occurs when the current density exceeds a certain threshold value. The GOI yield in percent is defined as the number of undamaged capacitors divided by the total number of test capacitors. Three breakdown modes have been defined, where A-mode failure is the early breakdown (electric field strength $E < 1 \text{ mV/cm}$), B-mode failures are the weak spots ($E = 1\text{--}8 \text{ mV/cm}$) and C-mode failure is the intrinsic breakdown ($E > 8 \text{ mV/cm}$). The effect of grown-in defects and metallic impurities on the gate oxide quality is described by the B-mode yield. The C-mode yield includes all the other origins for GOI yield degradation mentioned above. An additional method is the charge-to-breakdown Q_{bd} -test, where a fixed current is forced through the test capacitor until the system fails. Under the assumption of a perfectly random defect distribution (Poisson statistics), the GOI defect density (GOI-DD) can be calculated as a logarithmic function of GOI yield and area of a test capacitor.

Another aspect of gate oxide quality is its time-dependent behavior. This is measured by the so-called time-dependent dielectric breakdown (TDDB) test, in which either constant or ramped voltages or currents are applied [159].

Gate oxide degradation (in particular, B-mode failure) has been attributed directly to defects observed with all the above techniques, further strengthening the viewpoint that they share common origins [122,123,160,161] (Fig. 2). The impact of grown-in defects on oxide breakdown depends on the thickness of the oxide layer as well [162,163]. It has been found empirically that oxide layers 40–50 nm thick are most susceptible to grown-in defects. Thinner oxides show higher GOI yields, and, at a thickness of 5 nm thickness, the influence of the substrate grown-in defect density on the GOI yield becomes negligible [164].

Wafers from CZ grown vacancy-rich ingots reach TZDB GOI yields from 5% to more than 80%, depending on the hot zone and the pull rate, if the capacitor area is about 0.1 cm^2 and the gate oxide is about 25 nm thick. Nitrogen doped with respect FZ and epi wafers are superior to GOI yield with yields up to 100%. COP nuclei, present in substrate wafers, do not degrade the GOI yield on

epitaxial wafers, because epi layers with thickness of several microns are much thicker than the typical size of a COP [165]. Methods to improve the GOI yield of CZ wafers after ingot growth include thermal annealing at around 1200°C in argon or hydrogen ambients [166–168]. The mechanism of this ‘passivation’ is not fully understood. GOI yield improvements from about 30 to above 95% have been achieved using this technique, but the method is costly and not suitable for large diameter wafers (especially for 300 mm) because of thermal stress generation.

5.3. Modeling and prediction of void formation

The discussion above highlights the importance of understanding how processing conditions lead to void formation and growth during crystal growth and wafer processing. This has led to numerous efforts aimed at simulating directly the formation of vacancy aggregation in order to link quantitatively the thermal and growth conditions during growth to the observed D-defect distribution in CZ crystals. Ironically, a significant number of these models were developed based on the (incorrect) assumption that D-defects were small oxide precipitates. We mention these studies here because, in most cases, a simple adjustment of the rate expressions for the aggregation process was all that was necessary to adapt these models to the simulation of void evolution. In fact, void formation is a much simpler system to study because of the absence of significant strain effects in the matrix silicon and the absence of a second chemical species.

The first model aimed at computing the size distribution of D-defects explicitly as a function of thermal annealing schedules did in fact assume that these microdefects were oxide precipitates and is described in Schrems et al. [169] and Esfandyari et al. [26]. The numerical method used by these authors was similar to the one described in this paper; a FPE was used to describe the size distribution for clusters larger than several atoms, while discrete rate equations were used for each of the smallest few clusters. Their model was subsequently modified to investigate vacancy aggregation and was used in some of the above calculations to compute the void size distribution as a function of crystal growth conditions; see Dornberger [118] for details.

Nakamura et al. [170] used the point defect dynamics model of Habu et al. [22] to describe point defect diffusion and recombination and added an expression for the steady-state classical homogeneous nucleation flux in which the free energy driving force is computed from the supersaturation of vacancies and the size of the clusters. Their results predicted the same qualitative behavior for the void size distribution as our model once small adjustments to the original point defect properties are made. A major assumption of the analysis of Nakamura et al. was that point defect diffusion to the clusters is sufficient to maintain classical nucleation and that a diffusion-limited regime is not established. The validity of this criterion would be subject to the processing conditions. Voronkov and Falster [177] also have developed models for vacancy aggregation in CZ crystal growth and wafer thermal annealing. In addition to detailed numerical modeling, they have derived closed-form approximate expressions for void size distributions and densities based on the classical homogeneous nucleation theory.

While the above models differ in the parameterization of thermophysical properties and in the numerical techniques used to solve the various partial differential equations, it is important to note the global use of homogeneous nucleation theory to describe the point defect aggregation process and also to note its apparent success as will be demonstrated in the following sections. In fact, simple homogeneous nucleation arguments have now been used to describe the formation of more complex microdefects including the broad category of oxide precipitates which we do not focus on in this article. We now describe the details and results of our own model for void formation. The model is essentially an extension of the point defect dynamics model discussed in Section 4 which now

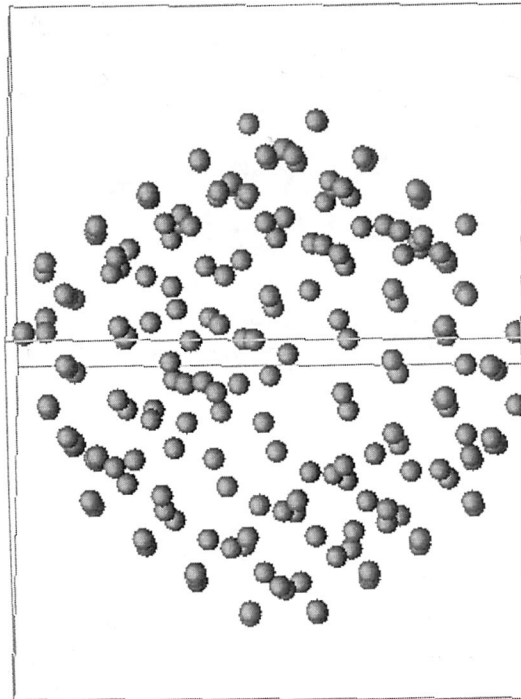


Fig. 17. Low-coordination atoms surrounding a 275-vacancy void showing the faceting of the defect surface oriented along the $\langle 111 \rangle$ directions. Overall shape is octahedral.

includes explicitly the nucleation and growth of vacancy aggregates, based on the modeling framework described in Section 2.

An important aspect of our study is the self-consistency of the model induced by preserving all the point defect properties used to describe OSF-ring dynamics. We isolate a single additional parameter needed to complete our model. Eq. (2.14) describes classically the free energy of formation of microdefects in terms of volumetric and surface contributions. In the case of vacancy aggregates, the volumetric term is identically 0 and the total free energy can be expressed in terms of the surface parameter, σ_v . The evidence that voids are faceted along the $\{111\}$ crystallographic directions as shown in Fig. 17 is used to interpret the void surface energy in terms of the energy of the Si- $\{111\}$ surface. There are several estimates for the Si- $\{111\}$ surface energy and we use here $\sigma_v = 1.0 \text{ J/m}^2$, an average of several literature values. Our own theoretical estimate [18] for this parameter of 1.25 J/m^2 , obtained with the SW interatomic potential, is in reasonably good agreement with this value.

Clearly, the above macroscopic representation of a void is not accurate for very small voids of, say, tens of vacancies. For this reason, we use atomistic simulation to compute the free energies of very small clusters and match these results with the continuum representation; see Sinno and Brown [49] for a detailed description. In this way, we are assured of self-consistency with respect to the point defect properties discussed in Section 4. Another method for describing small cluster free energies has been proposed recently by Voronkov and Falster [171], where two-dimensional nucleation is found to be dominant for very small clusters and greatly slows nucleation rates for these clusters, resulting in a 'lag-time' between small cluster nucleation and large cluster growth.

The remainder of this section is arranged as follows. The general features of a prototypical result are discussed in terms of the evolution of both the vacancy and aggregate concentration fields.

The results are then compared with actual void size distribution data using consistent thermal fields computed for an experimental CZ system, as described in Section 3. All the results described below are obtained with one-dimensional simulations, in which a single radial position is identified and used to compute the axial point defect and aggregate evolution. Radial profiles are computed using a sequence of one-dimensional calculations. The validity of a one-dimensional approximation is justified for regions not close to the crystal surface, based on the point defect flux analysis described in Section 4.

5.3.1. Prototypical results for defect evolution under vacancy-rich conditions

There are various features in the computations that are common to all situations where vacancy-rich conditions exist during growth. These are discussed here for a sample simulation, denoted as HS1/4. The one-dimensional temperature field used in this calculation corresponds to the temperature along the centerline of a 4" ingot grown at a pull rate of 1.8 mm/min. The results for aggregate density are reported in terms of the integral of all void sizes greater than 50 nm in diameter (or about 3×10^6 vacancies); we refer to this quantity as N_{50} . This value is selected based on the experimental detection limit, thereby making our predictions comparable directly to experimental measurements. Even so, voids as small as a few nanometers in diameter are thought to affect critical device properties such as GOI [118]; we also report the quantity N_5 , which corresponds to the sum of the number of all voids greater than 5 nm in diameter (about 3×10^3 vacancies). There is a little ambiguity in defining this quantity, however, because such voids tend to be highly unstable with respect to thermal processing and are likely to dissolve at intermediate temperatures. Therefore, whether they contribute to GOI performance is unclear and the actual threshold may depend on previous processing conditions.

The axial profile predicted as a function of crystal temperature for both N_5 and N_{50} is shown in Fig. 18 for the base case described above. Two features are notable; both measures of void density give almost identical final void densities. This is fortunate, given the ambiguity discussed above. The second feature, which is more difficult to see, is that the concentration of voids becomes appreciable

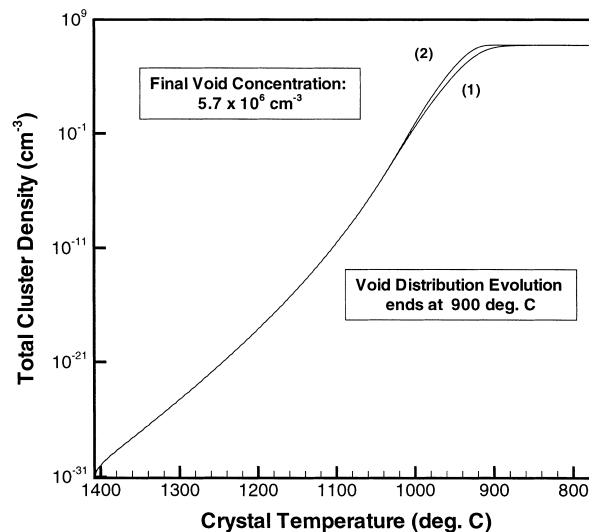


Fig. 18. Spatial evolution of the total void density defined by (1) all clusters larger than 5 nm and (2) all clusters larger than 50 nm.

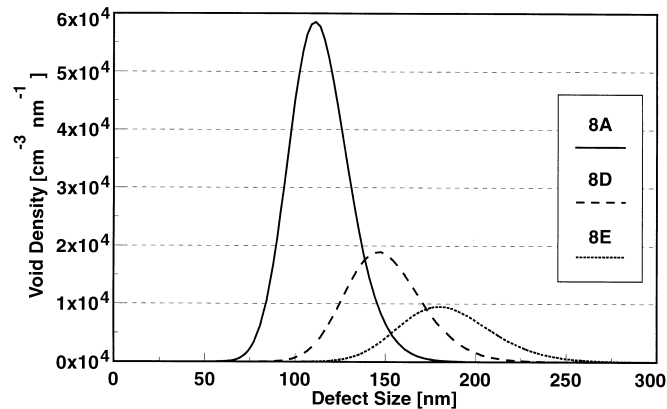


Fig. 19. Size distribution for voids binned into diameter intervals of 1 nm.

and reaches its final value across a very narrow temperature interval; this feature is somewhat hidden because of the exponential scaling used in Fig. 18.

Typical size distributions for three 8 in. crystals grown under different cooling conditions are shown in Fig. 19. An important point to note here is the arbitrariness of the ordinate; we show here and in all subsequent plots the concentration of voids per 1 nm interval in diameter. The peak height in the size distribution will increase as larger intervals are used. This is an important consideration, especially in the context of comparison with experiment. We find for this example that the peaks in the size distribution occur at diameter of about 100–175 nm, depending on the thermal conditions during growth.

Crystal 8A was grown under the fastest cooling conditions, while crystal 8E was grown in a slow cooling environment. The evolution of the size distribution with decreasing cooling rate is readily understood in terms of classical Ostwald ripening [172]. As the cooling rate is decreased, more time is available for evolution of the size distribution, in which larger aggregates grow at the expense of smaller, less stable ones. This process occurs solely by the dynamic exchange of single vacancies between the individual voids because they are immobile and far too dilute to interact by other mechanisms such as coalescence. Thus, in all crystal growth situations, the resulting aggregate size distribution is determined by kinetics, rather than thermodynamics; none of the observed size distributions correspond to equilibrium profiles.

Voids are found typically in concentrations of up to about $1 \times 10^5 \text{ cm}^{-3}$ with slow cooled crystals having significantly lower densities of about $1 \times 10^4 \text{ cm}^{-3}$. This range is typical for most crystal growth operating conditions. An important part of defect engineering is to balance the void size and density in order to achieve an optimal GOI. The remainder of this section focuses on quantifying the effect of crystal growth processing conditions on these values.

5.3.2. Thermal history effects on void size distribution

The technological relevance of voids in CZ silicon has led to numerous efforts aimed at describing quantitatively the dependence of size distribution on various segments of the crystal thermal history during crystal growth. Dornberger and coworkers [118,173] have correlated GOI, which is a direct measure of void density, to a temperature range of $1173 \text{ K} \leq T \leq 1323 \text{ K}$ by performing a regression analysis for the entire crystal cooling history. Fig. 20 shows the GOI defect density as a function of dwell time in the temperature range $1173 \text{ K} \leq T \leq 1323 \text{ K}$ for a broad range of hot zone configurations and crystal radii and demonstrates the importance of this segment of the thermal history in setting the overall void density within the as-grown crystal.

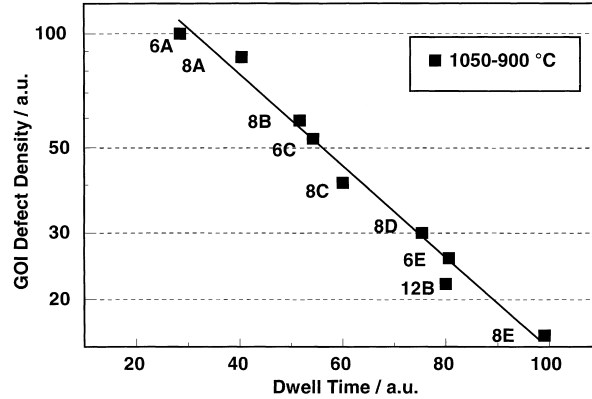


Fig. 20. GOI defect density as a function of dwell time in the temperature interval $1050^{\circ}\text{C} \geq T \geq 900^{\circ}\text{C}$ for crystals grown in different thermal environments and radii.

Other estimates for the so-called nucleation temperature range have been published in the literature. Takano et al. [174] provide a higher temperature range, $1353\text{ K} \leq T \leq 1423\text{ K}$, which is also narrower than the estimate of Dornberger et al., implying that the onset of rapid void nucleation and growth is even faster. Harada et al. [175] assumed incorrectly that LSTDs were oxide precipitates and reported a nucleation temperature range of $1363\text{ K} \leq T \leq 1433\text{ K}$ in good agreement with the measurement of Takano et al. Hourai et al. [176] reported a similar range of $1273\text{ K} \leq T \leq 1423\text{ K}$ for measured LSTD densities, but have also attributed the LSTD to an oxygen-related defect. The experiments of Nakamura et al. [170] show that the range $1153\text{ K} \leq T \leq 1453\text{ K}$ is most relevant for setting the final void concentrations and size distribution. Finally, Voronkov and Falster [177] have presented a detailed analysis of void nucleation and conclude that the temperature range is extremely narrow, about 5 degrees, and that onset occurs at about 1343 K.

The very narrow nucleation and growth onset temperature feature is also apparent from our simulation results as shown in Fig. 18. The large scatter reported in the literature for the onset of void nucleation is best understood in the context of Fig. 21, which divides crystal into four regions (R1–R4), based on the evolution of the vacancy and void concentrations. R1 has already been discussed in the context of the evolution of the OSF-ring and the very rapid point defect recombination that characterizes this region. We also note here the formation of near-equilibrium

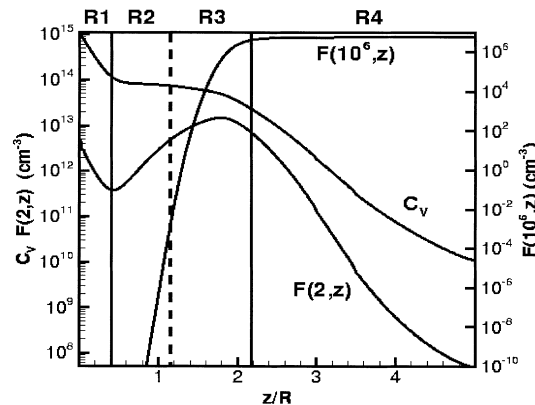


Fig. 21. Decomposition of the crystal thermal history in terms of the evolution of single-vacancy and vacancy cluster concentrations.

concentrations of small vacancy aggregates, namely dimers and trimers, which have negligible effect on the total vacancy concentration. A portion of these small aggregates redissolves as the concentration of vacancies is reduced by recombination.

In R2, the vacancy profile is flat because recombination ceases as the self-interstitial concentration is depleted. In addition, the supersaturation of vacancies is still too small to cause appreciable formation of critical nuclei. This is achieved in the narrow R3 region where the concentration of critical voids is sufficiently large so as to cause a rapid depletion of single vacancies. Cluster growth is accompanied by the dissolution of smaller, less stable nuclei that provide vacancies for the growth of large, stable aggregates; this process is characteristic of coarsening. Finally, the region R4 shows a fully developed void size distribution that has essentially consumed most of the available vacancies. The still decreasing vacancy concentration is too small to cause appreciable changes in the void size distribution in this region.

An important consideration in this analysis is the sequential nature of the microscopic processes that lead to the formation of a given size distribution of voids. The thermal field in the regions of the crystal near the melt/crystal interface sets the post-recombination vacancy concentration. These vacancies are then available for aggregation. This implies that the thermal field in the region immediately next to the melt/crystal interface contributes to the final observed void size distribution through the level of the vacancy supersaturation. In fact, as demonstrated in Section 4, the post-recombination vacancy concentration is not only a function of the thermal environment but also depends on the pull rate, according to the V/G criterion described there. Thus, while the cooling rate (or $V \times G$) is critical at lower temperatures, the important parameter is V/G at temperatures near the melting point. This composite dependence likely explains the wide range of nucleation temperatures reported in the literature because it is unlikely that the different cooling rate experiments were performed with a fixed thermal field at the melt/crystal interface; hence, the level of vacancy supersaturation varies with the experiments.

Our simulation results are most consistent with the analysis and results of Voronkov and Falster [177]. The discrepancy in the actual temperature at which void nucleation is most significant is most likely due to the prescribed thermophysical properties used in our simulations. The source of uncertainty in most simulation predictions tends to stem from the vacancy properties, particularly the vacancy free energy of formation; we believe that this parameter is most likely to produce the variations observed.

The evolution of microdefects in a vacancy-rich crystal is summarized in Fig. 22, using a ‘phase diagram’ representation, with the ‘state variables’ being the vacancy concentration and the temperature. We find empirically that the onset of void formation takes place when the vacancy concentration reaches approximately 10 times the value of the local equilibrium concentration. Thus, in the regions near the melt/crystal interface, recombination with self-interstitials leads to vacancy supersaturation faster than the effect of the decreasing temperature of the crystal with axial position. After the self-interstitials are depleted, the supersaturation increases until it reaches the critical level for initiating void aggregation. The onset of oxygen precipitation at a lower temperature (850°C) also is shown in Fig. 22. While it is not our intent to focus explicitly on the phenomenon of oxygen precipitation here, it is important to mention in this context because, at lower temperatures, oxygen precipitation competes with void formation for single vacancies. Thus, in situations where void nucleation is delayed or otherwise limited, the vacancy concentration remaining for oxide precipitation can actually be higher than in regions where void formation is extensive.

In fact, the dependence of oxide precipitation on the vacancy concentration provides an explanation for the narrow annular structure of the OSF-ring. Near the crystal center, the residual vacancy concentration after recombination is high, and corresponds to a high value of V/G . In this

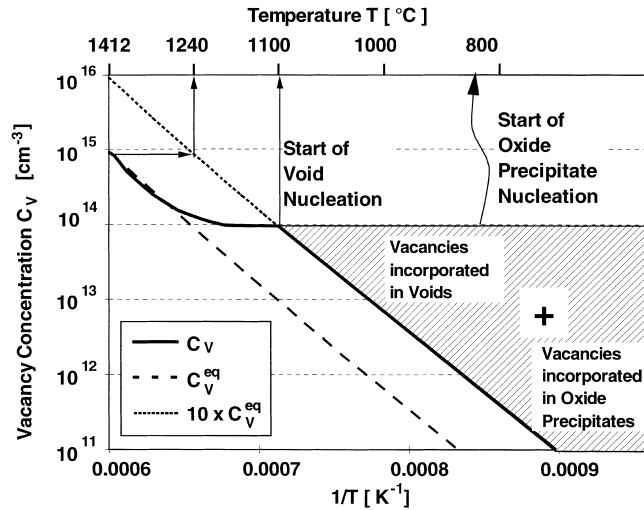


Fig. 22. 'Phase diagram' based on the vacancy levels in a crystal as a function of thermal history.

region, the vacancy supersaturation reaches the critical level for nucleation at a relatively high temperature. Then, there is plenty of time for void formation to take place while the temperature is sufficiently high. The final vacancy concentration remaining for oxide precipitation is therefore quite low and few precipitates are seen here.

Near the crystal's radial surface, V/G is below the critical value and self-interstitials deplete the vacancy population and both void and oxide precipitation processes are inhibited. However, in a narrow region, vacancies survive the recombination phase in numbers that are too low for significant void formation to take place. Our simulations show in fact that this region contains the most single vacancies at temperatures near the onset of oxide precipitation, thus leading to a localized region of high oxide precipitate density. These precipitates are thought to be the nuclei for the interstitial-type stacking faults that constitute the OSF-ring. This mechanism also is discussed in [178].

5.3.3. Radial structure of the void size distribution

An important measure of wafer quality is the radial uniformity of the microdefect. To probe this structure, a series of one-dimensional calculations were performed, each with a thermal field extracted at a different radial position within the crystal. The results shown in Fig. 22 are for an 8 in. crystal grown under slow cooling conditions, which leads to a vacancy-dominated crystal at all radial positions. Experimental measurements for the void size distribution also are shown in Fig. 22 as a function of radial position. The 'total' predicted void density is given in Fig. 13 and is defined to correspond with experimentally visible voids with diameters of about $0.1 \mu\text{m}$. Two important features emerge from this figure. The first is the presence of a peak in the density close to the crystal rim before it drops sharply to very small values. In the crystal interior, the density is approximately constant at an intermediate value.

These distributions can be explained qualitatively by considering simultaneously point defect recombination and the subsequent void nucleation. In the interior portions of the crystal, the parameter V/G is high, and a large supersaturation of vacancies is left after recombination depletes the self-interstitial population. At these radial positions, nucleation starts early in the crystal thermal history and the size distribution has ample time to coarsen, forming a population that is distributed across both small and large void aggregates. As the crystal is traversed radially, V/G is reduced while remaining above the critical value, which implies that the surviving vacancy population is less

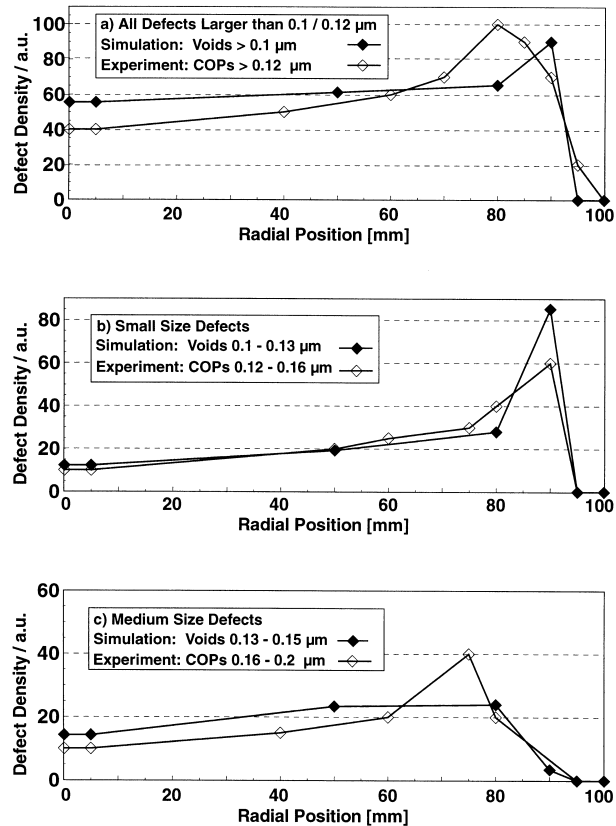


Fig. 23. Radial variation of simulated grown-in voids and COPs (a) for all sizes above 0.1–0.12 μm , (b) for small, and (c) for medium sizes in crystal 8D.

supersaturated at a given temperature as compared to interior radial positions. Hence, nucleation begins at a lower temperature and the void size distribution has less time to coarsen, resulting in the presence of a large number of small voids and very few larger ones. The process of coarsening is known to reduce the overall density as many small voids are typically consumed in order to grow a single larger one. Very close to the crystal's radial surface, the balance between interstitials and vacancies is such that very few vacancies survive recombination, essentially preventing the onset of homogeneous nucleation at any temperature during crystal growth; then, no voids are observed. The presence of such a region depends on the crystal growth conditions.

Evidence for this picture is shown in Figs. 23 and 24, where a plot comparing the measured and predicted densities for different segments of the size distribution is shown. A sharply peaked region

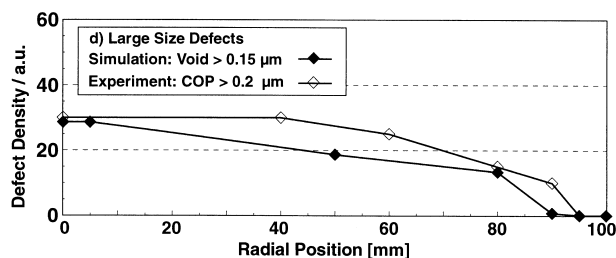


Fig. 24. Radial variation of simulated grown-in voids and COPs for all sizes larger than 0.15–0.2 μm in crystal 8D.

near the crystal rim is shown in Fig. 23b; this peak contains many smaller voids. The concentration of voids of size 0.1–0.13 μm in the crystal interior, however, is quite low as the coarsening process is allowed to proceed. The next segment of the size distribution is shown in Fig. 23c for voids of size 0.13–0.15 μm . The same overall profile is observed with a less pronounced peak near the rim and a higher intermediate value in the interior portion. Fig. 24 shows the radial profile for voids larger than 0.15 μm . The profile for this segment of the size distribution is qualitatively different than the rest, in that the density rises monotonically towards the center of the crystal. Clearly, large voids require sufficient coarsening time and a large number of vacancies, both of which are more closely related to the value of V/G near the melt/solid interface than the remainder of the cooling history. The fact that they appear in lower densities as compared to the smaller voids implies that the overall radial profile will primarily be influenced by the distribution of small voids as shown in Fig. 23a.

5.4. Self-interstitial aggregation

While the focus of this article is directed towards the modeling and prediction of vacancy aggregation, the process of self-interstitial aggregation is closely related and is outlined briefly below. Some current potential approaches for producing void-free crystalline silicon involve intermediate steps in which the as-grown crystal is self-interstitial rich [179]. In these situations, the ability to predict conditions for the onset of self-interstitial cluster nucleation and growth is important.

Several experimental characterizations of self-interstitial aggregates have been reported in the literature [180]. Self-interstitial clustering leads to the formation of large dislocation loop clusters with diameters up to several microns. These have been observed in swirl patterns as revealed by X-ray topography following Cu or Li decoration [181,182]. Such defects are commonly known as *A-swirl* defects and are large enough to have been observed by TEM [181]. Smaller self-interstitial aggregates, known as *B-defects* have also been observed by X-ray topography followed by decoration, but these are too small to be viewed directly with TEM. They are believed to be three-dimensional precursors to *A-defects*. Qualitative models [181] for self-interstitial aggregation postulate that the initial stages of self-interstitial aggregation are aided by the presence of carbon atoms, which supply free volume. Once these aggregates reach a certain size, they become unstable relative to other morphologies, such as extrinsic stacking faults, and finally, dislocation loops. The precise mechanism for self-interstitial aggregation remains an open question.

Mori [183] has performed the most detailed calculations of self-interstitial aggregation to date by considering a fully coupled point defect dynamics model in which both self-interstitials and vacancies are allowed to diffuse, recombine, and aggregate. The aggregation model for self-interstitials includes a compound free energy function, which predicts a transition from three-dimensional aggregates to stacking faults to dislocation loops as each aggregate grows. Crystals grown under self-interstitial rich conditions, i.e. for V/G values below the critical value given in Eq. (4.3), have been observed [184] to undergo self-interstitial aggregation at around 950–1030°C. Using a fitting parameter to set the ratio between the surface and volumetric contributions to the free energy of formation of spherical clusters, Mori obtains good agreement with experimentally observed aggregation onset temperatures.

While typical densities of extrinsic dislocation loops, $O(10^4\text{--}10^5\text{ cm}^{-3})$, are lower than those of voids for similar respective point defect supersaturation levels, the enormous size of the dislocation loop clusters imposes a ‘zero-tolerance’ rule on the presence of self-interstitial clusters in silicon wafers, and is one of the reasons why, until recently, there has been little interest in growing Si crystals under these conditions.

5.5. Summary and conclusions

The results presented here demonstrate that the understanding of microdefect formation in crystalline silicon is now sufficiently detailed to allow for fairly accurate predictions for densities and size distributions as a function of crystal growth operating conditions. Most importantly, it has been amply demonstrated that the origin of technologically important microdefects, such as voids, is directly connected to the detailed spatial evolution of native point defects — vacancies and self-interstitials. The most important result of the model described in this Section is that the final microdefect distribution within an as-grown crystal is a function of most of the thermal history of the crystal, even though the exact nature of this coupling differs in the various regions. In particular, it has been demonstrated that the relevant parametric group near the melt/crystal interface is the ratio of the crystal growth rate to the axial temperature gradient at the interface (V/G). The radial structure observed in both FZ and CZ crystals is due almost entirely to the implicit radial dependence of the interfacial axial temperature gradient, i.e. $G=G(r)$. This parameter V/G essentially determines the type and level of point defects that remain once recombination is halted due to the depletion of one of the point defect species. The remaining point defects become rapidly supersaturated as the crystal cools and lead to the nucleation of the corresponding microdefect type. At this stage of microdefect evolution, it is the cooling rate that is important in setting the final size distribution, here expressed as $V \times G'$ where the prime notation denotes that the gradient is an average defined over the temperature region in the crystal in which nucleation and aggregation is important.

For vacancies, a model based on diffusion-limited homogeneous nucleation describes quantitatively the final void size distribution over a wide range of crystal growth conditions and is self-consistent with respect to the prediction of OSF-ring dynamics based on point defect concentrations. It is also encouraging to note that this agreement is obtained by describing void energies in terms of the $\langle 111 \rangle$ silicon surface, which removes the need for additional parameterization of the free energy of the voids. A weakness that remains in this approach is that it is unable to generate an accurate estimate for the free energies of small vacancy clusters, which are only a few lattice spacings in characteristic length. It is highly unlikely that these clusters resemble anything like the mesoscopic octahedral voids that are observed experimentally and therefore will have significantly different energies than the values predicted by simple extrapolation of the $\langle 111 \rangle$ surface model. Some estimates for these energies based on detailed atomistic simulation have begun to appear [185] and show non-monotonic variation of the formation energy as a function of size. The effect of such predictions on results of microdefect simulation needs to be evaluated in more detail.

6. Conclusions

The analysis of point defect and microdefect dynamics in crystalline silicon is currently at a crossroads. The developments in the last 5 years have set the framework for enormous advances in our understanding and have attracted very significant industrial interest because of the obvious technological importance of the results in microelectronic device fabrication. Simultaneously, the calculations are just becoming predictive resulting in quantitative predictions of changes in the microdefect distributions with operating conditions. An open issue is whether detailed simulation of microdefect dynamics during crystal growth and subsequent materials processing can replace the extensive experimental investigation that has been the basis for most real processing in silicon crystal growth and device processing. These traditional efforts are not based on a complete understanding

of microscopic phenomena, but instead on empirical process–property relationships that guide development and process optimization.

The issue of void minimization during crystal growth is a classic example. Despite the fact that the origin of ‘D-defects’ was not known until recently, operating conditions for reducing the defect concentration have been discovered empirically. A systematic sensitivity analysis implemented experimentally would then lead to an operating window in which acceptable yields of high quality crystal was achieved. This approach has led to a spectacular, and unrelenting, technological development rate over the last 30 years. However, it is also apparent that the push for modeling within the industry is becoming more urgent. This increasing interest stems from the increased accuracy of the descriptions, made possible by sophisticated numerical solution and the quantitative linkage of these predictions to experiment. The research described in this article and the references herein show conclusively that quantitatively useful information now can be obtained from simulation.

The other incentive for adopting modeling-based development is more of a compulsory one; devices are becoming larger and feature lengths are becoming smaller. The combination of these two trends leads to the need to understand defects that are only a few atoms in size at concentrations that are measured in the 10^3 cm^{-3} range and to analysis of very large-scale processing systems. In crystal growth, larger diameter Czochralski systems mean that the expense associated with experiments is rapidly becoming a limiting factor for development. This is a very real issue with the growth of 12 in. diameter ingots where the radial defect distribution in these ingots is significantly more inhomogeneous than in smaller diameter crystals. The optimization of thermal fields for these crystals will likely be almost entirely performed using global thermal simulations like the one described in Section 3. Even so, it is not even clear that the microdefect distribution in the polished wafers will be a viable competitor against wafers with epitaxial silicon layers because of the required operating conditions anticipated for optimizing the void distribution in the large diameter substrates [186].

Most, but not all, of the mechanistic processing of point defects that are responsible for void formation and dissolution are understood, as is their link to crystal growth and thermal annealing conditions. The models discussed above in Section 5 contain the essential physical mechanisms needed to predict void formation as a function of crystal pull rate and thermal history. However, it is much less safe to say that we have a predictive tool that can replace experiment. The persistent issue of accurate thermophysical property estimation continues to limit the usefulness of most silicon process models today. Both traditional approaches, diffusion measurements and atomistic simulation are still incapable of supplying point defect, let alone cluster, properties that are sufficiently accurate for use in defect dynamics models without fitting to experiment. It is an unfortunate peculiarity of silicon that self-interstitial and vacancy properties are similar and lead to very sensitive models that require highly accurate values for the properties of these defects.

With thermophysical property estimation being so important it seems prudent to focus on this issue in future work in this area. A promising approach is model integration, in which several, preferably weakly correlated, defect dynamics phenomena are considered simultaneously based on the same, or at least overlapping, parameter sets. This approach can provide stringent tests leading to a narrowing of the allowable range on each fitting parameter. For example, such an approach would require that the very same self-interstitial and vacancy properties used to model boron diffusion during wafer annealing, would also reproduce OSF-ring dynamics and void size distributions. The work described in this article is a first step at such integration. Once point defect properties are fit to OSF-ring dynamics, these properties are fixed in the subsequent model for vacancy aggregation. This implies a much-reduced number of parameters in any subsequent fitting procedures. The fact that

semi-quantitative agreement for the void size distribution can be obtained without additional fitting of the void surface energy is a strong indication that the essential physics for these phenomena are being included in our model.

Whatever the best approach, it is clear that more rigorous methods for thermophysical property estimation must be developed before we can truly say that computer simulation of crystal growth and wafer processing is successful. A particular challenge lies in the study of the initial stages of microdefect nucleation. These species tend to exist on very short timescales as clusters grow to increase their thermodynamic stability and are therefore impossible to image and characterize with conventional techniques. Furthermore, these microdefects pose difficult challenges for theoretical investigation. Atomistic simulations are limited by the number of atoms that can be considered and by the time scales accessible in the simulation. Current methods for bypassing these difficulties include the use of macroscopic phenomenological descriptions for the cluster free energy curve all the way down to clusters containing only a few atoms. The advent of more sophisticated ‘mesoscopic’ simulation tools will improve this particular aspect in the near future.

Despite these limitations, simulation is poised as an important tool for realistic simulation of microdefect formation in silicon, particularly for native point defect and aggregate species that contain mainly self-interstitials and vacancies. Coupled with accurate global thermal models for the Czochralski crystal growth system, the area of defect engineering for crystal growth and device processing has been born.

Acknowledgements

We thank MEMC Corporation, SEMATECH, Shin-Etsu Handotai, and Wacker Siltronic AG for financial support of this research. One of us (TS) also thanks the University of Pennsylvania Research Foundation.

References

- [1] J. Czochralski, *Zs. Phys. Chemie* 92 (1918) 219.
- [2] T.S. Plaskett, *Trans. Met. Soc. AIME* 233 (1965) 809.
- [3] T. Abe, in: N.G. Einspruch, H. Huff (Eds.), *VLSI Electronics: Microstructure Science*, Vol. 12, Academic Press, New York, 1985.
- [4] P.M. Fahey, P.B. Griffin, J.D. Plummer, *Rev. Mod. Phys.* 61 (1989) 289.
- [5] L.A. Girifalco, *Statistical Physics of Materials*, Wiley, New York, 1973.
- [6] G.H. Vineyard, *Phys. Chem. Solids* 3 (1957) 121.
- [7] D. Maroudas, R.A. Brown, *Appl. Phys. Lett.* 62 (1993) 172.
- [8] P.B. Rasband, P. Clancy, M.O. Thompson, *J. Appl. Phys.* 79 (1996) 8998.
- [9] T.R. Waite, *Phys. Rev.* 107 (1957) 463.
- [10] D.A. Antoniadis, I. Moskowitz, *J. Appl. Phys.* 53 (1982) 9214.
- [11] A. Seeger, K.P. Chik, *Phys. Stat. Solidi* 29 (1968) 455.
- [12] T. Sinno, R.A. Brown, E. Dornberger, W. von Ammon, *J. Electrochem. Soc.* 145 (1998) 303.
- [13] T. Sinno, *Defects in crystalline silicon: integrated atomistic and continuum modeling*, Ph.D. Thesis, Massachusetts Institute of Technology, Cambridge, MA, 1998.
- [14] A. Seeger, H. Foll, W. Frank, in: N.B. Urli, J.W. Corbett (Eds.), *Radiation Effects in Semiconductors 1975*, IOP, Bristol, 1977.
- [15] T. Sinno, Z.K. Jiang, R.A. Brown, *Appl. Phys. Lett.* 68 (1995) 3028.
- [16] M. Volmer, A. Weber, *Z. Physik. Chem.* 119 (1925) 277.
- [17] J. Katz, J.H. Wiedersich, *J. Chem. Phys.* 55 (1971) 1414.
- [18] T. Sinno, F.K. von Gottberg, R.A. Brown, *J. Comput.-Aid. Mater. Des.* 4 (1997) 29.
- [19] A. Bongiorno, L. Colombo, *Appl. Phys. Lett.*, 2000, submitted for publication.
- [20] S.R. deGroot, P. Mazur, *Non-equilibrium Thermodynamics*, Dover, New York, 1984.

- [21] W. Wijaranakula, J. Electrochem. Soc. 140 (1993) 3306.
- [22] R. Habu, A. Tomiura, Jpn. J. Appl. Phys. 35 (1996) 1.
- [23] W.A. Tiller, M. Friedman, R. Shaw, N. Cuendet, T. Halicioglu, J. Crystal Growth 186 (1998) 113.
- [24] I.M. Lifshitz, V.V. Slyozov, J. Chem. Phys. Solids 19 (1961) 35.
- [25] H. Risken, The Fokker–Planck Equation: Methods of Solution and Applications, Springer, Berlin, 1984.
- [26] J. Esfandiyari, C. Schmeiser, S. Senkader, G. Hobler, B. Murphy, J. Electrochem. Soc. 143 (1996) 995.
- [27] C.DeW. Van Siclen, W.G. Wolfer, Acta Metall. Mater. 40 (1992) 2091.
- [28] S.M. Hu, J. Appl. Phys. 57 (1985) 1069.
- [29] H. Zimmermann, H. Ryssel, Appl. Phys. A 55 (1992) 121.
- [30] N.A. Stolwijk, J. Holzl, W. Frank, E.R. Weber, H. Mehrer, Appl. Phys. A 39 (1986) 37.
- [31] T.Y. Tan, U. Gosele, Appl. Phys. A 37 (1985) 1.
- [32] H. Bracht, N.A. Stolwijk, H. Mehrer, Phys. Rev. B 52 (1995) 16542.
- [33] S.M. Hu, J. Appl. Phys. 45 (1974) 1567.
- [34] P.B. Hirsch, A. Howie, R.B. Nicholson, D.W. Pashley, Electron Microscopy of Thin Crystals, Butterworths, London, 1965.
- [35] S. Dannefaer, P. Mascher, D. Kerr, Phys. Rev. Lett. 56 (1986) 2195.
- [36] D. Frenkel, B. Smit, Understanding Molecular Simulation, Academic Press, San Diego, 1996.
- [37] R. Car, M. Parinello, Phys. Rev. Lett. 55 (1985) 2471.
- [38] P.E. Blochl, E. Smargiassi, R. Car, D.B. Laks, W. Andreani, S.T. Pantelides, Phys. Rev. Lett. 70 (1993) 2435.
- [39] F.H. Stillinger, T.A. Weber, Phys. Rev. B 31 (1985) 5262.
- [40] J. Tersoff, Phys. Rev. B 37 (1988) 6991.
- [41] J. Tersoff, Phys. Rev. B 38 (1998) 9902.
- [42] M.Z. Bazant, E. Kaxiras, J.F. Justo, Ohys. Rev. B 56 (1997) 8542.
- [43] J.F. Justo, M.Z. Bazant, E. Kaxiras, V.V. Bulatov, S. Yip, Rhys. Rev. B 58 (1998) 2539.
- [44] H.R. Schober, Phys. Rev. B 39 (1989) 13013.
- [45] H. Balamane, T. Halicioglu, W.A. Tiller, Phys. Rev. B 46 (1992) 2250.
- [46] P.Y. Yu, M. Cardona, Fundamentals of Semiconductors, Springer, Berlin, 1996.
- [47] P.B. Rasband, P. Clancy, M.O. Thompson, J. Appl. Phys. 79 (1996) 8998.
- [48] C.Z. Wang, C.T. Chan, K.M. Ho, Phys. Rev. Lett. 66 (1991) 189.
- [49] T. Sinno, R.A. Brown, J. Electrochem. Soc. 146 (1999) 2300.
- [50] T. Mori, Ph.D. Thesis, Massachusetts Institute of Technology, Cambridge, 2000.
- [51] C. Johnson, Numerical Solutions of Partial Differential Equations by the Finite Element Method, Cambridge University Press, Cambridge, 1987.
- [52] J.S. Chang, G. Cooper, J. Comput. Phys. 6 (1970) 1.
- [53] G. Teal, IEEE Trans. Electron Devices 23 (1976) 621.
- [54] D. Hurler, in: E. Kaldis (Ed.), Crystal Growth of Electronic Materials, Elsevier, Amsterdam, 1985, p. 3.
- [55] W. Zulehner, D. Huber, in: J. Grabmeier (Ed.), Crystals & Silicon Chemical Engineering, Springer, Berlin, 1982.
- [56] D.T.J. Hurle, B. Cockayne, in: D.T.J. Hurle (Ed.), Handbook of Crystal Growth, Vol. 2, North-Holland, Amsterdam, 1994, p. 99.
- [57] G.K. Teal, J.B. Little, Phys. Rev. 78 (1950) 647.
- [58] W. Dash, J. Appl. Phys. 30 (1959) 459.
- [59] R.B. Bird, W.E. Stewart, E.N. Lightfoot, Transport Phenomena, Wiley, New York, 1960.
- [60] A. Seidl, “Über den Einfluß der Tegelrotation auf den Wärme- und Stofftransport in Halbleiter-schmelzen bei Czochralski”, Universität Erlangen Dissertationsschrift, 1995.
- [61] R.W. Johnson, Handbook of Fluid Mechanics, Springer, Heidelberg, 1998 (Chapter 14).
- [62] A. Lipchin, R.A. Brown, J. Crystal Growth 205 (1999) 71.
- [63] A. Lipchin, R.A. Brown, Hybrid finite-volume/finite-element simulation of heat transfer and turbulence in Czochralski crystal growth of silicon, J. Crystal Growth, 2000, in press.
- [64] A. Lipchin, R.A. Brown, Hybrid finite-volume/finite-element simulation oxygen segregation in Czochralski silicon growth, J. Crystal Growth, 2000, submitted for publication.
- [65] J.J. Derby, R.A. Brown, J. Crystal Growth 83 (1987) 183.
- [66] A. Wheeler, J. Crystal Growth 56 (1982) 67.
- [67] A. Murgai, H. Gatos, A. Witt, J. Electrochem. Soc. 123 (1976) 224.
- [68] K. Yi, H. Chung, H. Lee, J. Yoon, J. Crystal Growth 132 (1993) 451.
- [69] S. Kobayashi, S. Miyahara, T. Fujiwara, T. Kubo, H. Fujiwara, S. Inami, J. Crystal Growth 180 (1997) 334.
- [70] S. Kobayashi, J. Crystal Growth 99 (1990) 692.
- [71] N. Kobayashi, T. Arizumi, Jpn. J. Appl. Phys. 9 (1970) 361.
- [72] T. Arizumi, N. Kobayashi, J. Crystal Growth 13/14 (1972) 615.
- [73] S. Miyahara, S. Kobayashi, T. Fujiwara, T. Kubo, H. Fujiwara, Proceedings of the Sixth International Symposium on Silicon Materials Science and Technology, Semiconductor Silicon, 1990, Pennington, USA, Electrochem. Soc. 1990, pp. 94–104.

- [74] M. Crochet, P. Wouters, F. Geyling, A. Jordan, J. Crystal Growth 65 (1983) 153.
- [75] F. Dupret, Y. Ryckmans, P. Wouters, M.J. Crochet, J. Crystal Growth 79 (1986) 84.
- [76] F. Dupret, P. Nicodeme, Y. Ryckmans, P. Wouters, M. Crochet, Int. J. Heat Mass Transfer 33 (1990) 1849.
- [77] F. Dupret, N. van den Bogaert, in: D. Hurle (Ed.), Handbook of Crystal Growth, North-Holland, Amsterdam, 1994, p. 875.
- [78] R. Brown, T. Kinney, P. Sackinger, D. Bornside, J. Crystal Growth 97 (1989) 99.
- [79] L. Atherton, J.J. Derby, R. Brown, J. Crystal Growth 84 (1987) 57.
- [80] D. Bornside, T. Kinney, R. Brown, G. Kim, Int. J. Numer. Methods Eng. 30 (1990) 133.
- [81] J.J. Derby, R.A. Brown, F.T. Geyling, A.S. Jordan, G.A. Nikolakopoulou, J. Electrochem. Soc. 132 (1985) 470.
- [82] J.J. Derby, R.A. Brown, J. Crystal Growth 87 (1988) 251.
- [83] J.J. Derby, L. Atherton, P. Thomas, R.A. Brown, J. Sci. Comput. 2 (1987) 297.
- [84] A.B. Crowley, IMA J. Appl. Math. 30 (1983) 173.
- [85] D. Hurle, G. Joyce, M. Ghassempoor, A. Crowley, E. Stern, J. Crystal Growth 100 (1990) 11.
- [86] K. Kim, A. Kran, P. Smetana, G. Schwuttke, J. Electrochem. Soc. 130 (1983) 1156.
- [87] C. Hwang, K. Chen, S. Lin, J. Crystal Growth 147 (1995) 390.
- [88] N. Van den Bogaert, F. Dupret, J. Crystal Growth 171 (1997) 65.
- [89] N. Van den Bogaert, F. Dupret, J. Crystal Growth 171 (1997) 77.
- [90] P. Ramachandran, M. Dudukovic, J. Crystal Growth 71 (1985) 399.
- [91] G. Williams, R. Reusser, J. Crystal Growth 64 (1983) 448.
- [92] M. Hamidi, C. Belouet, J. Crystal Growth 82 (1987) 22.
- [93] O. Anttila, M. Tilli, V. Lindroos, Mater. Res. Soc. Symp. Proc. 59 (1985) 323.
- [94] S. Schmitt, Diplomarbeit, Universität Erlangen/Nürnberg, 1995.
- [95] K. Brattkus, S. Davis, J. Crystal Growth 87 (1988) 385.
- [96] R. Howell, J. Siegel, Thermal Radiation Heat Transfer, Taylor & Francis, Hemisphere, Washington, DC, 1992.
- [97] N. van den Bogaert, Ph.D. Thesis, UCL, Louvain-la-Neuve, Belgium, 1993.
- [98] P. Wouters, Ph.D. Thesis, UCL, Louvain-la-Neuve, Belgium, 1985.
- [99] N. van den Bogaert, Ph.D. Thesis, UCL, Louvain-la-Neuve, Belgium, 1993.
- [100] W. von Ammon, E. Dornberger, H. Oelkrug, H. Widener, J. Crystal Growth 151 (1995) 273.
- [101] M. Hasebe, Y. Takeoka, S. Shinoyama, S. Naito, Jpn. J. Appl. Phys. 28 (1989) 1999.
- [102] T. Abe, H. Harada, in: S. Mahajan, J.W. Corbett (Eds.), Defects in Semiconductors II, North-Holland, New York, 1983.
- [103] T. Abe, H. Harada, Mater. Res. Soc. Symp. Proc. 14 (1983) 1.
- [104] E. Dornberger, W. von Ammon, J. Electrochem. Soc. 143 (1996) 1648.
- [105] K. Sueoka, M. Akatsuk, K. Nishihara, T. Yamamoto, S. Kobayashi, Mater. Sci. Forum 196–201 (1995) 1737.
- [106] V.V. Voronkov, J. Crystal Growth 59 (1982) 625.
- [107] A.J.R. de Kock, Appl. Phys. Lett. 16 (1970) 100.
- [108] P.M. Petroff, A.J.R. de Kock, J. Crystal Growth 35 (1976) 4.
- [109] P.J. Roksnoer, M.M.B. van den Boom, J. Crystal Growth 53 (1981) 563.
- [110] H. Foll, U. Gosele, B.O. Kolbesen, J. Crystal Growth 52 (1981) 907.
- [111] W. von Ammon, P. Dreier, W. Hensel, U. Lambert, L. Koster, Mater. Sci. Eng. B 36 (1996) 33.
- [112] V.V. Voronkov, R. Falster, J.C. Holzer, Electrochem. Soc. Proc. PV 97-22, 1997, p. 3.
- [113] R. Habu, K. Kawakami, M. Hasebe, Solid State Phenom. 57/58 (1997) 27.
- [114] R. Habu, Jpn. J. Appl. Phys. 36 (1997) 2800.
- [115] T. Ebe, J. Crystal Growth 203 (1999) 387.
- [116] A.M. Agrawal, S.T. Dunham, J. Appl. Phys. 78 (1995) 5313.
- [117] U. Gosele, T.Y. Tan, in: S. Mahajan, J.W. Corbett (Eds.), Defects in Semiconductors II, North-Holland, New York, 1983.
- [118] E. Dornberger, Prediction of OSF-ring dynamics and grown-in voids in Czochralski silicon crystals, Ph.D. Thesis, Universite Catholique de Louvain, 1999.
- [119] M. Itsumi, H. Akiya, T. Ueki, M. Tomita, M. Yamawaki, J. Appl. Phys. 78 (1995) 10.
- [120] M. Itsumi, H. Akiya, M. Tomita, T. Ueki, Japanese Journal Appl. Phys. Part 1, 35 (1996) 812–817.
- [121] M. Itsumi, H. Akiya, T. Ueki, M. Tomita, M. Yamawaki, Jpn. J. Appl. Phys. 35 (1996) 812.
- [122] J. Park, G. Rozgonyi, Solid State Phenom. 47/48 (1996) 327.
- [123] J. Park, J. Park, K. Cho, G. Lee, H. Chung, in: Proceedings of the Second International Symposium on Advanced Science and Technology of Silicon Materials, 1996, p. 519.
- [124] H. Yamagishi, I. Fusegawa, K. Takano, E. Iino, N. Fujimaki, T. Ohta, M. Sakurada, in: Proceedings of the Semiconductor Silicon 1994, Electrochem. Soc. Proc. 94-10, 1994, p. 124.
- [125] J. Ryuta, E. Morita, T. Tanaka, Y. Shimanuki, Jpn. J. Appl. Phys. 29 (1990) L1947.
- [126] K. Moriya, T. Ogawa, Jpn. J. Appl. Phys. 22 (1983) 307.
- [127] M. Suhren, D. Gräf, R. Schmolke, H. Piontek, P. Wagner, Inst. Phys. Conf. Ser. 149 (1996) 301.

- [128] J. Vanhellemont, E. Dornberger, J. Esfandiyari, G. Kissinger, M.-A. Trauwaert, H. Bender, D. Gräf, U. Lambert, W.V. Ammon, Trans. Tech. Publications, Switzerland, Mater. Sci. Forum, 258–263 (1), (1997) 341–346.
- [129] M. Kato, H. Takeno, Y. Kitagawara, Proceedings of the MRS Fall Meeting, Defects in Electronic Materials II, Mater. Res. Soc., Pittsburgh, USA, 1997, p. 119.
- [130] H. Yamagishi, I. Fusegawa, N. Fujimaki, M. Katayama, Semicond. Sci. Technol. 7 (1992) A135.
- [131] W. Wijaranakula, J. Electrochem. Soc. 141 (1994) 3273.
- [132] H. Takeno, M. Kato, Y. Kitagawara, in: Proceedings of the Second International Symposium on Advanced Science and Technology of Silicon Materials, 1996, p. 302.
- [133] E. Morita, J. Ryuta, T. Tanaka, Y. Shimanuki, Chemical Surface Preparation, Passivation and Cleaning for Semiconductor Growth and Processing Symposium, Mater. Res. Soc., Pittsburgh, PA, USA, 1992, pp. 161–166.
- [134] E. Morita, H. Okuda, F. Inoue, in: Proceedings of the Semiconductor Silicon 1994, Electrochem. Soc. Proc. 94-10, 1994, p. 156.
- [135] M. Miyazaki, S. Miyazaki, Y. Yanase, T. Ochiai, Jpn. J. Appl. Phys. 34 (1995) 6303.
- [136] M. Brohl, D. Gräf, P. Wagner, U. Lambert, H. Gerber, H. Piontek, in: Proceedings of the ECS Fall Meeting, Miami Beach, Vol. 94-2, Abstract No. 403, 1994, p. 619.
- [137] J. Vanhellemont, G. Kissinger, K. Kenis, M. Depas, D. Gräf, U. Lambert, P. Wagner, High Technology 17, NATO ASI Series, Vol. 3, Kluwer Academic Publishers, Dordrecht, 1996, p. 493.
- [138] K. Moriya, T. Ogawa, Jpn. J. Appl. Phys. 22 (1983) 307.
- [139] K. Moriya, K. Hirai, K. Kashima, S. Takasu, J. Appl. Phys. 66 (1989) 5267.
- [140] J. Fillard, J. Crystal Growth 103 (1990) 71.
- [141] J. Furukawa, H. Furuya, T. Shingyouji, Jpn. J. Appl. Phys. 32 (1993) 5178.
- [142] M. Hourai, T. Nagashima, E. Kajita, S. Miki, T. Shigematsu, J. Electrochem. Soc. 142 (1995) 3193.
- [143] G. Kissinger, J. Vanhellemont, D. Gräf, C. Claeys, H. Richter, Inst. Phys. Conf. Ser. 149 (1996) 19.
- [144] G. Kissinger, J. Vanhellemont, D. Gräf, W. Zulehner, C. Claeys, H. Richter, in: B.O. Kolbesen, C. Claeys, P. Stallhofer (Eds.), Proceedings of the Satellite Symposium to ESSDERC 95 The Hague, ALTECH 95, The Electrochem. Soc. PV 95-30, 1995.
- [145] W. Bergholz, W. Mohr, W. Drewes, Mater. Sci. Eng. B 4 (1989) 359.
- [146] R. Winkler, G. Behnke, in: Proceedings of the Semiconductor Silicon 1994, Electrochem. Soc. Proc. 94-10, 1994, p. 973.
- [147] R. Winkler, M. Sano, J. Electrochem. Soc. 141 (1994) 1398.
- [148] S. Kim, W. Wijaranakula, J. Electrochem. Soc. 142 (1995) 553.
- [149] S. Kim, W. Wijaranakula, J. Electrochem. Soc. 141 (1994) 1872.
- [150] M. Miyazaki, S. Miyazaki, T. Kitamura, T. Aoki, Y. Nakashima, M. Hourai, T. Shigematsu, Jpn. J. Appl. Phys. 34 (1995) 409.
- [151] D. Gräf, M. Brohl, S. Bauer-Mayer, A. Ehlert, P. Wagner, A. Schnegg, Mater. Res. Soc. Symp. Proc. 315 (1993) 50.
- [152] P. Mertens, H. Schmidt, M. Meuris, S. Verhaverbeke, D. Gräf, K. Dillenbeck, S. Salem, M. Heyns, in: 1993 Symposium on VLSI Technology, Digest of Technical Papers (IEEE Cat. No. 93CH 3303-5), Bus. Center for Acad. Soc., Tokyo, Japan, 1993, pp. 111–112.
- [153] M. Morita, A. Teramoto, K. Makiyara, T. Ohmi, Y. Nakazato, A. Uchiyama, T. Abe, in: Proceedings of the Third International Symposium on Ultra Large Scale Integration Science and Technology, ULSI Science and Technology 1991, Electrochem. Soc., Pennington, NJ, 1991, pp. 400–408.
- [154] M. Meuris, M. Heyns, P. Mertens, S. Verhaverbeke, A. Philipossian, Cleaning Technol. Semicond. Develop. Manuf., Electrochem. Soc. Proc. PV 92-12, 1992, p. 144.
- [155] T. Kitano, E. Hasegawa, M. Tsukkiji, K. Akimoto, S. Kimura, S. Saito, K. Ikeda, Jpn. J. Appl. Phys. 32 (1993) 1583.
- [156] R. Thakur, N. Chhabra, A. Ditali, Appl. Phys. Lett. 64 (1994) 3428.
- [157] E. Sottocasa, F. Illuzzi, D. Nahmad, M. Polignano, Semiconductor Silicon 1994, Electrochem. Soc. Proc. 94-10, 1994.
- [158] M. Itsumi, O. Nakajima, N. Shiono, J. Appl. Phys. 72 (1992) 2185.
- [159] K. Yoneda, K. Okuma, K. Hagiwara, Y. Todokoro, J. Electrochem. Soc. 142 (1995) 596.
- [160] T. Shiota, E. Morita, T. Shingyouji, Y. Shimanuki, Electrochem. Soc. Abstract No. 793 (1993).
- [161] Y. Satoh, T. Shiota, Y. Murakami, T. Shingyouji, H. Furuya, J. Appl. Phys. 79 (1996) 7944.
- [162] M. Itsumi, J. Electrochem. Soc. 141 (1994) 2460.
- [163] J. Park, S. Choi, G. Lee, Y. Jeong, Y. Kwak, C. Shin, S. Hahn, W. Smith, P. Mascher, in: Electrochemical Society Proceedings, Spring Meeting, St. Louis, 1992.
- [164] U. Lambert, A. Huber, J. Grabmeier, G. Obermeier, J. Vanhellemont, R. Wahlich, G. Kissinger, Microelectron. Eng. 48 (1999) 127.
- [165] D. Gräf, private communication, 1992.
- [166] W. Wijaranakula, Appl. Phys. Lett. 64 (1994) 1.
- [167] D. Gräf, U. Lambert, M. Brohl, A. Ehlert, R. Wahlich, P. Wagner, J. Electrochem. Soc. 142 (1995) 3189.
- [168] D. Gräf, U. Lambert, M. Brohl, A. Ehlert, R. Wahlich, P. Wagner, Mater. Sci. Eng. B 36 (1996) 50.
- [169] M. Schrems, T. Brabec, M. Budil, H. Potzl, E. Guerrero, D. Huber, P. Pongratz, Mater. Sci. Eng. B 4 (1989) 393.

- [170] K. Nakamura, T. Saishoji, T. Kubota, T. Iida, Y. Shimanuki, T. Kotooka, J. Tomioka, *J. Crystal Growth* 180 (1997) 61.
- [171] V.V. Voronkov, R. Falster, *J. Crystal Growth* 198/199 (1999) 399.
- [172] W. Ostwald, *Z. Phys. Chem.* 37 (1901) 385.
- [173] E. Dornberger, J. Esfandiyari, D. Graf, J. Vanhellemont, U. Lambert, F. Dupret, W. von Ammon, in: B.O. Kolbesen, P. Stallhofer, C. Claeys, F. Tardiff (Eds.), *Crystalline Defects and Contamination: Their Impact and Control in Device Manufacturing II*, *Electrochem. Proc. Ser. PV 97-22*, Pennington, NJ, 1996, p. 40.
- [174] K. Takano, K. Kitagawa, M. Kimura, H. Yamagishi, *Mater. Sci. Forum* 196 (1995) 1707.
- [175] K. Harada, H. Furuya, M. Kida, *Jpn. J. Appl. Phys.* 36 (1997) 3366.
- [176] M. Hourai, T. Nagashima, E. Kajita, S. Miki, T. Shigematsu, *J. Electrochem. Soc.* 142 (1995) 3193.
- [177] V.V. Voronkov, R. Falster, *J. Crystal Growth* 194 (1998) 76.
- [178] R. Falster, V.V. Voronkov, *J. Crystal Growth* 204 (1999) 462.
- [179] R. Falster, Low Defect Density, Self-interstitial Dominated Silicon, Patent No. PCT/US 98/07365.
- [180] H. Foll, U. Goesele, B.O. Kolbesen, *J. Crystal Growth* 40 (1977) 90.
- [181] H. Foll, B.O. Kolbesen, *Appl. Phys.* 8 (1975) 319.
- [182] P.M. Petroff, A.J.R. de Kock, *J. Crystal Growth* 30 (1975) 117.
- [183] T. Mori, Modeling the linkages between heat transfer and microdefect formation in crystal growth: examples of Czochralski growth of silicon and vertical Bridgman growth of bismuth germanate, Ph.D. Thesis, Massachusetts Institute of Technology, Cambridge, 2000.
- [184] T. Saishouji, K. Nakamura, H. Nakajima, T. Yokoyama, F. Ishikawa, J. Tomioka, High purity silicon V, *Electrochem. Soc. Proc. Ser.*, 1998, p. 28.
- [185] A. La Magna, S. Coffa, L. Colombo, *Mater. Res. Soc. Symp. Proc.* 538 (1999) 241.
- [186] W. von Ammon, E. Dornberger, P.O. Hansson, *J. Crystal Growth* 390 (1999) 198–199.